Materials Chemistry and Physics 329 (2025) 130107

Contents lists available at ScienceDirect

Materials Chemistry and Physics

journal homepage: www.elsevier.com/locate/matchemphys

Full length article

A novel approach for Tool-Narayanaswamy-Moynihan model parameter extraction using multi-scale neural model

Marek Pakosta[a], Petr Dolezel[a,*], Roman Svoboda[b]

[a] Department of Automation and Mathematics, Faculty of Electrical Engineering and Informatics, University of Pardubice, Studentska 95, Pardubice, 53210, Czech Republic
[b] Department of Physical Chemistry, Faculty of Chemical Technology, University of Pardubice, Studentska 95, Pardubice, 53210, Czech Republic

GRAPHICAL ABSTRACT

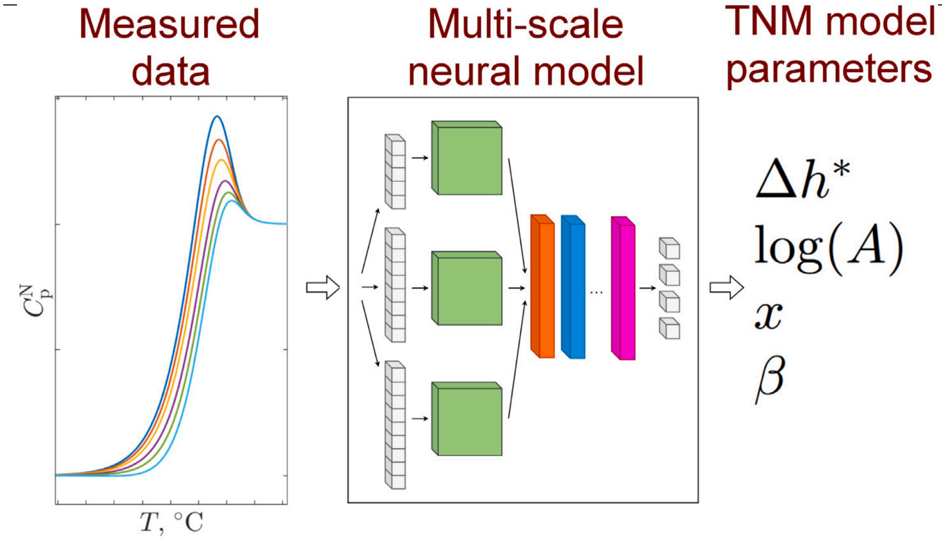

HIGHLIGHTS

- Machine learning was used to model and describe the glass transition kinetics.
- A novel MCNN architecture accurately estimates relaxation parameters of TNM model.
- Training and testing was done for 13.7 million theoretically simulated samples.
- The accuracy and precision of MCNN matches or surpasses the traditional methods.
- The proposed MCNN exhibits a superior computational efficiency.

ARTICLE INFO

Dataset link: https://numcraft.eu

Keywords:
Tool-Narayanaswamy-Moynihan model

ABSTRACT

The accurate determination of parameters in the Tool-Narayanaswamy-Moynihan (TNM) model, which describes the viscoelastic behavior of glass-forming materials, is crucial for predicting material responses through various thermal histories. Traditional methods rely heavily on curve-fitting techniques; however, these

---

* Corresponding author.
E-mail addresses: marek.pakosta@student.upce.cz (M. Pakosta), petr.dolezel@upce.cz (P. Dolezel), roman.svoboda@upce.cz (R. Svoboda).

https://doi.org/10.1016/j.matchemphys.2024.130107
Received 30 June 2024; Received in revised form 17 October 2024; Accepted 30 October 2024

Multi-scale neural model
Enthalpy relaxation dynamics
Glass transition
Differential scanning calorimetry

often fail due to noise in the data. Furthermore, traditional methods are computationally intensive and prone to inaccuracies, particularly when dealing with complex datasets or when the initial parameter guesses are far from optimal; also, they require a skilled personnel.

In this study, we propose the application of a multi-scale convolutional neural network (MCNN) as a machine learning approach to address these challenges. The MCNN model is trained on a comprehensive simulated dataset encompassing a wide range of TNM parameters, allowing it to learn intricate patterns and dependencies within the data that are difficult to capture with conventional methods. Our results show that the MCNN significantly improves the accuracy of the parameter estimations for β and x across the entire spectrum of tested conditions, achieving performance that is not only comparable to, but often surpasses, traditional curve-fitting methods. Furthermore, the MCNN demonstrates superior robustness when initial parameter estimates are suboptimal or when the dataset exhibits significant noise. Although the prediction accuracy for the activation energy Δh^* and the pre-exponential factor $\log(A)$ was somewhat lower, the method still provides valuable estimates that can be refined with supplementary techniques.

This work highlights the potential of machine learning approaches like MCNN to revolutionize the parameter extraction process in complex physical models, reducing the reliance on manual curve-fitting and providing a more automated, scalable solution. We also analyze the primary sources of prediction errors in the MCNN outputs and offer insights into future improvements, including model architecture refinements and the integration of additional physical constraints. Our findings suggest that this approach can be extended to other domains where similar models are employed, paving the way for broader applications of machine learning in materials science.

1. Introduction

Glass transition is a physico-chemical phenomenon occurring in all amorphous materials [1–3]. It is a transition between the states of under-cooled liquid and glass, where the structure of the material becomes gradually denser during cooling to the point when its compactness prevents further densification.

The crucial importance of this phenomenon is given by the fact that this transition (usually characterized by the so-called glass transition temperature, T_g) is associated with large changes in mechanical, electrical, optical, and many other properties [4–6]. Above T_g, the material is soft and pliant, whereas below T_g, the molecular structure becomes frozen-in and the material behaves as a hard but fragile solid. The glass transition behavior is, on a molecular level, dictated by the process of structural relaxation, which summarizes the manifestations of the movements of the relevant structural entities during their progressive re-ordering in the given temperature range. The kinetics of these movements then determine not only the position of the phenomenon on the temperature scale but also its width (rate of the change between the two borderline structural states), sensitivity to the applied cooling/heating rate, and overall complexity of the structural changes associated with the transition. Apart from this information being crucial for the practical utilization of all amorphous materials (be it state-of-the-art hi-tech optoelectronic applications [7–13] or the classical engineering within, e.g., the glass and polymer industries [14–19]), the kinetics of glass transition is also considered one of the most important yet not fully understood phenomena of solid-state physics and chemistry [20–22]. In particular, the exact nature of the relaxation motions and the intensity of their macroscopic manifestations need to be correlated with the chemical composition (inorganic glasses), molecular structures (low-molecular organic glasses), and even super-molecular structures (polymers). A deeper understanding of these relationships would enhance the overall perception of the mutual links between solid-state chemistry and physics.

The Tool-Narayanaswamy-Moynihan (TNM) model is a cornerstone in the field of glass science, particularly due to its robust ability to describe the non-equilibrium kinetics of structural relaxation during glass transition. This model is integral to understanding the temporal evolution of glassy systems as they approach equilibrium from a non-equilibrium state, which is a fundamental aspect of material science. The importance of the TNM model arises from its comprehensive treatment of the relaxation process, which accounts for the complex interplay between time, temperature, and structural state in glass-forming materials.

One of the key strengths of the TNM model is its incorporation of both the time-dependent and non-linear nature of structural relaxation. The model captures the decelerating kinetics of the relaxation process as the material cools through the glass transition, where the relaxation time increases exponentially with decreasing temperature. These features of the structural relaxation process (denoted as non-linearity and non-exponentiality) are of utmost importance, as they dictate the rapidity and magnitude of the structural changes occurring during the transition between the glassy and undercooled liquid states. The ability to follow, utilize and predict the glass transition temperature window and the timescales associated with the relaxation motions is essential for the short-term processing of glassy materials (molding, fiber-drawing, stress-reducing annealing, avoiding the nucleation processes or the diffusion-less sub-T_g crystal growth in pharmaceutical substances, etc.), as well as for the accounting for the long-term changes of numerous physico-chemical properties reflecting the slow relaxation processes well below T_g. As such, the accurate and full description of all structural relaxation features (achieved via the TNM model) is crucial not only for the prediction of the glassy material behavior under varying thermal conditions, but also for the compositional/composite fine-tuning of the materials' properties with regard to the intended application.

Moreover, the TNM model's ability to describe the glass transition in terms of a single set of parameters, that are consistent across different experimental conditions, provides a unifying framework for understanding glass relaxation. This consistency is essential for the development of predictive models that can be applied across different materials and conditions, facilitating advancements in material design and processing [23–25].

The canonical form of the TNM model is defined as follows:

$$\frac{T_f(t)-T_f(\infty)}{T_f(0)-T_f(\infty)} = \exp\left[\left(\int_0^t \frac{dt}{\tau}\right)^{\beta}\right], \tag{1}$$

$$\tau(T,T_f) = A\exp\left[x\frac{\Delta h^*}{RT} + (1-x)\frac{\Delta h^*}{R_g T_f}\right], \tag{2}$$

where T_f is the so-called fictive temperature [23] (defined as a temperature of the undercooled liquid with the same structure as that of the relaxing glass at the given moment), the indices 0 and ∞ correspond to the initial and final equilibrium states respectively, t is time, T is temperature, τ is relaxation time, R_g is the universal gas constant, Δh^* is the apparent activation energy of structural relaxation, A is the pre-exponential constant, $x \in (0 < x < 1)$ is the non-linearity parameter, and $\beta \in (0 < \beta < 1)$ is the non-exponentiality parameter. In practice, T_f from Eq. (1) is replaced by the experimentally recorded physical quantity. Whereas the structural relaxation process can be observed through a large number of physical quantities, the calorimetric measurements are probably the most convenient instrumentation, given their accuracy, precision, accessibility of the experimental equipment, and zero requirements regarding the sample pre-processing. In particular, differential scanning calorimetry (DSC) [26], which records heat flow ϕ proportional to the material's heat capacity C_p, is considered a standard technique for studying the glass transition kinetics. Since the heat capacity is obtained as a second derivative of the Gibbs free energy with respect to temperature, it relates to T_f (which corresponds to the first derivative) via the following equation:

$$C_\mathrm{p}^\mathrm{N} = \frac{C_\mathrm{p} - C_\mathrm{pg}(T)}{C_\mathrm{pl}(T) - C_\mathrm{pg}(T)} = \frac{\mathrm{d}T_\mathrm{f}}{\mathrm{d}T}, \tag{3}$$

where C_p^N is the normalized relaxation signal; $C_\mathrm{pg}(T)$ and $C_\mathrm{pl}(T)$ denote the inter/extrapolated temperature dependences of the heat capacity in the glassy and liquid states, respectively. Note that despite certain shortcomings [27] with regard to the description of deeply relaxed states, the TNM model is, to this date, the most popular and often used set of equations for the direct description of the calorimetric and volumetric structural relaxation data in the glass transition range.

The determination of the glass transition kinetics in terms of the TNM model subsists in the enumeration of Eqs. (1) and (2), i.e., in the evaluation of the four TNM parameters: A, Δh^*, x, and β. The methodological approaches for the determination of the TNM parameters from the derivative/calorimetric experimental data were summarized in [28]. These methodologies generally fall into three categories: nonlinear curve-fitting, linearization methods, and simulation-comparative techniques. However, all three of these approaches have certain flaws. The curve-fitting is extremely sensitive to even slight distortions of the measured signal [28]. The linearization methods were derived only for two out of the four TNM parameters: h_R and x (where the determination of x requires the execution of specific, extremely long experimental measurements). The evaluations based on the simulation comparative methods are time-demanding, requiring an iterative approach via brute computing force. Given these limitations, the exploration of alternative approaches, such as artificial neural networks (ANNs), for the evaluation of the TNM parameters holds great promise. Since ANNs excel in recognizing hidden and complex patterns, large advancement can be expected with regard to the reliability and accuracy of the TNM parameter determination – especially in the (relatively common) cases, where the traditional methods fail, i.e., for the distorted, noisy or weak relaxation signals. The potentially highly increased accuracy and resolution of the TNM parameter determination would then allow for, so far infeasible, disclosure of fine compositional trends in the structural relaxation behavior of glassy materials [28,29]. Consequently, physico-chemical interpretation of these trends and their association with the occurrence of certain types of structural units would greatly improve the fine-tuning options in the development of new glassy materials.

Nowadays, deep learning and artificial neural networks have become an integral part of research as well as common life. In their most sophisticated forms, ANNs are capable of pushing the boundaries of what was previously thought possible, leading to groundbreaking applications that span various domains. One of the most prominent applications of deep learning is in image recognition and processing. Advanced convolutional neural networks (CNNs) are capable of outperforming humans in tasks like object recognition [30], facial recognition [31], and even medical image analysis [32]. ANNs also excel in natural language processing [33], autonomous vehicles [34], financial predictions [35], climate modeling [36], robotics [37], and creative content generation [38].

In recent years, Multi-scale Convolutional Neural Networks (MCNNs) have rapidly gained traction as a state-of-the-art approach in the domain of signal analysis, offering unparalleled capabilities for extracting meaningful features from complex data. The multi-scale nature of MCNNs is particularly advantageous for handling the diverse and intricate characteristics of signals associated with structural relaxation. By processing the input data at multiple scales, MCNNs can efficiently capture both fine-grained details and broader patterns that are critical for accurate parameter extraction [39,40]. This ability to operate across various spatial and temporal resolutions ensures that MCNNs can adapt to the inherently multi-scale nature of the relaxation phenomena, thereby enabling a more precise and comprehensive extraction of relevant parameters.

Furthermore, the resilience of MCNNs to noise and parasitic signals, as highlighted in recent studies [41], makes them especially effective in real-world applications where data can often be imperfect or contaminated. This robustness is crucial when dealing with experimental data that may be subject to various sources of noise, ensuring that the extracted parameters remain reliable and accurate.

Given the increasing complexity of modern signal processing tasks and the need for advanced analytical techniques, the application of MCNNs represents a cutting-edge approach that aligns perfectly with the demands of contemporary material science research. Their abilities provide a powerful tool for extracting the intricate parameters of the TNM model, making them an ideal choice for this task. As such, the use of MCNNs in this context not only leverages the latest advancements in deep learning but also offers a robust and sophisticated method for advancing the understanding of the glass transition process.

While ANNs have been increasingly utilized in various fields of thermal analysis [42], their application has largely been restricted to predicting thermoanalytical data, processing such data, and performing thermokinetic analysis [43–46]. Nonetheless, with regard to the glass transition, ANNs were strictly used to predict the position of T_g for various glassy and polymeric systems based on their chemical structure [47–51]. To the authors' best knowledge, no reports on ANN being used to extract the kinetic information directly from the structural relaxation data-curves exist in the literature.

The aim of the presented paper is to explore the ability of ANNs, specifically the multi-scale convolutional neural network, to estimate the TNM structural relaxation parameters (A, Δh^*, x, and β) based on the standard (normalized) derivative relaxation/calorimetric signals (see Eq. (3) and Fig. 1(b)), or relaxation signals for short. The input training data will be theoretically simulated with high accuracy and with an ambitious goal, to cover the absolute majority of types of structural relaxation behavior occurring for real-life materials. The performance of MCNN will be evaluated using several metrics – most importantly, the sums of squared estimates of errors SSE calculated for the $\frac{\mathrm{d}T_\mathrm{f}}{\mathrm{d}T}$ signals and for the weighted output TNM parameters. An optimized solution for the MCNN architecture capable of a reliable and accurate extraction of the TNM relaxation parameters from the calorimetric data will be introduced. The paper will represent a pilot work, mapping the base capability and potential bottleneck issues of the MCNN-based approach.

The decision to utilize a multi-scale convolutional neural network in this study is motivated by several key factors. Firstly, the MCNN architecture is particularly well-suited for analyzing signals that exhibit features across multiple scales, such as the derivative relaxation signals used for TNM parameter extraction. This multi-scale capability allows the network to effectively capture both local and global patterns within the data, which is crucial for accurately estimating parameters that govern the complex relaxation dynamics of glass-forming materials. Traditional machine learning approaches, such as shallow neural networks or simpler regression models, often struggle with such multi-scale data due to their limited ability to capture hierarchical features.

In comparison to conventional nonlinear optimization techniques, such as curve-fitting or simulation-comparative methods, MCNN offers several advantages. While traditional methods require significant manual intervention, including expert-defined initial parameter guesses and iterative refinement, the MCNN model autonomously learns intricate patterns from the data, reducing the reliance on manual preprocessing and expert knowledge. Furthermore, conventional methods are computationally intensive and prone to inaccuracies when the data is noisy or when initial parameter estimates deviate significantly from their true values. In contrast, MCNN is expected to demonstrate superior robustness to such challenges, as highlighted in recent studies where neural networks have successfully outperformed classical optimization techniques in parameter estimation tasks [52].

Thus, MCNN has the potential to represent a powerful, automated, and scalable alternative to conventional nonlinear optimization methods for TNM parameter extraction, providing both accuracy and efficiency.

2. Materials and methods

In this section, the systematic approach to designing the multi-scale neural model for the TNM model parameter estimation is outlined. The presented methodology can be summarized through a series of distinct steps, each crucial in constructing a robust and effective neural model tailored to the parameter extraction from a multi-channel signal. Beginning with data preprocessing and dataset creation, the architecture design is then delved into, with a highlight on the integration of multi-scale features as a key innovation. Subsequently, the training strategy and evaluation criteria are discussed, all of which contribute to the model's overall performance. Through a step-by-step exposition of these pivotal stages, a comprehensive insight into the methods employed in the presented work is offered in the following paragraphs.

2.1. Dataset creation

In the field of deep learning, the creation of a high-quality dataset is a critical and foundational step in the development of robust neural models. A dataset should provide the information necessary to learn patterns and relationships in the input space.

In the context of this study, the dataset is expected to consist of the set of inputs formed by the relaxation signals, and the set of outputs composed of corresponding quartets of TNM model parameters: A, Δh^*, x, and β.

In order to acquire sufficient data, the dataset is artificially computed using the algorithm for the Tool-Narayanaswamy-Moynihan curve-fitting procedure [53]. According to that algorithm, the expression for the non-isothermal steps is represented by

$$T_{f,n} = T_0 + \sum_{j=1}^{n} \Delta T_j \left\{ 1 - \exp\left[-\left(\sum_{k=j}^{n} \frac{\Delta T_k}{q_k \tau_k} \right)^{\beta} \right] \right\}, \tag{4}$$

where T_0 is the initial equilibrium temperature. The fictive temperature T_f in this equation is determined based on the Boltzmann superposition integral over time, which can also be replaced by a corresponding integral over temperature. In practice, the continuous cooling or heating is replaced by a sequence of n temperature jumps ΔT, followed by isothermal holds with duration determined by the cooling and heating rates $\Delta t = \frac{\Delta T}{q}$, as suggested in [53]. The magnitude of ΔT must be sufficiently small to ensure linearity. The self-retarding kinetics can be introduced by dividing the aging time into k sub-intervals and calculating T_f and τ at the end of each. The fictive temperature is then used to calculate the normalized relaxation signal $C_{\mathrm{p}}^{\mathrm{N}}$, as follows.

$$C_{\mathrm{p}}^{\mathrm{N}} = \frac{\mathrm{d}T_f}{\mathrm{d}T}. \tag{5}$$

The use of Eqs. (4) and (5) allows the implicit computation of the relaxation signals for a selected course of repeated heating and cooling of the sample. Nevertheless, this process is computationally intensive – calculating for one quartet of TNM model parameters requires around 10 min of computation on a high-end computer. This duration is primarily dictated by the $O(N^2)$ computational complexity inherent in the process, as can be observed upon closer examination of Eq. (4).

In order to perform said calculation to obtain relaxation signals of interest, a carefully designed temperature input program must be used.

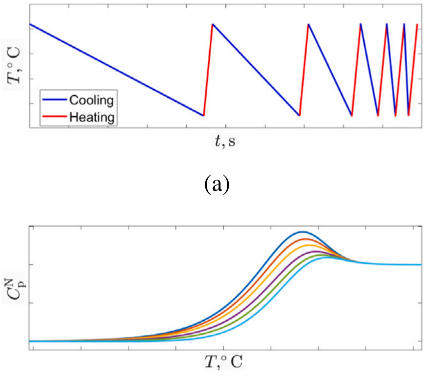

(a)

(b)

Fig. 1. Example of input temperature program – constant heating rate cycles (a). Example of output relaxation signals used in the dataset depending on both the input temperature program (b) & TNM model's A, Δh^*, x, and β values.

Table 1
Heating and cooling rates for individual CHR cycles.

#	Cooling from T_1 to T_0	Heating from T_0 to T_1
(1)	0.5 °C min^{-1}	10 °C min^{-1}
(2)	1 °C min^{-1}	10 °C min^{-1}
(3)	2 °C min^{-1}	10 °C min^{-1}
(4)	5 °C min^{-1}	10 °C min^{-1}
(5)	10 °C min^{-1}	10 °C min^{-1}
(6)	20 °C min^{-1}	10 °C min^{-1}

Typically, a standard temperature program is used for glass relaxation evaluation. This temperature program is represented by the so called constant heating rate (CHR) cycles, during which the sample is repeatedly cooled and heated through the glass transition region (Fig. 1(a)). In the CHR cycles temperature program, the cooling rates differ for each cycle, while the rate of heating stays always constant. Only a response of a system to the heating step is of practical interest and will be further visualized. However, the cooling steps are still an integral part of the simulations, because the relaxation behavior is influenced by the entire thermal history of the relaxing material – see integral in Eq. (1). For the purpose of this study, a set of six CHR cycles is taken – in accordance with the common practice [28] – as a typical representation of the material's relaxation response. Note that the material's response to the set of CHR cycles unambiguously determines (and is therefore unique for) a given combination of the TNM parameters (A, Δh^*, x, and β). Table 1 summarizes the cooling and heating rates used for the individual CHR cycles: T_1 and T_0 mark the upper and lower temperature boundaries of each set of CHR cycles, i.e., the initial temperatures of the cooling and heating steps, respectively. The T_1 and T_0 values are chosen so that the resulting output $C_{\mathrm{p}}^{\mathrm{N}}$ signals always reach the full glass ($C_{\mathrm{p}}^{\mathrm{N}} = 0$) and undercooled liquid ($C_{\mathrm{p}}^{\mathrm{N}} = 1$) states. A schematic example of the temperature profile and the $C_{\mathrm{p}}^{\mathrm{N}}$ response obtained during the heating steps of the CHR cycles set is depicted in Fig. 1(b).

Aside from the temperature program, the shape of relaxation signals is influenced by the four TNM parameters: A, Δh^*, x, and β in Eqs. (1) and (2). The creation of the dataset involves strategically designing the state-space of input parameters to comprehensively encompass the calculated glass transition behavior in the output. This meticulous approach ensures thorough coverage of the desired glass transition phenomena. Firstly, ranges of parameters are chosen in a continuous domain. These ranges are chosen on the basis of naturally occurring values in real amorphous materials and are listed in Table 2 below.

Since the width of the output signal is influenced mainly by parameters A and Δh^*, the state-space of these parameters is designed so that the output signal does not exceed the temperature range of

Table 2
TNM model parameters, their ranges & units.

Property	Range	Unit
$\log(A/s)$	$-18, -630$	–
Δh^*	$2\times10^5, 12\times10^5$	J mol^{-1}
x	$0.2, 1$	–
β	$0.2, 1$	–

$(-250, 1600)$ °C. In order to obtain a finite dataset, listed parameters are discretized. Firstly, Δh^* is discretized with a step size of 1e4 J mol^{-1}, effectively resulting in 101 discrete values. Secondly, each discrete Δh^* then specifies its range for A values, and in this range, 81 evenly spaced values are obtained; these A ranges are specified so that the output signal lies in the $(-250, 1600)$ °C temperature range. For brevity, these A ranges are not listed, but corresponding state space is visualized via scatter in the A-Δh^* plane shown in Fig. 3. As a result, $101 \times 81 = 8181$ A, Δh^* combinations are obtained. Fig. 2 comprises all combinations of A and Δh^*. On its own, a database with such coarsely discretized state space is unsuitable for any search-based optimization functions for determining/estimating the TNM parameters. However, taking into account the interpolation ability of ANNs, the state-space will be reasonably detailed to provide sufficient training data. Each A, Δh^* combination (cell in the table) then has its own combinations of x, β parameters. x and β range is discretized with a step of 0.02, as this step corresponds to a sufficient precision of the x and β exact determination (considering the potential ability to further interpolate to the 0.01 precision in each parameter). This results in 41 x and 41 β values; therefore, 1681 combinations are obtained for each A, Δh^* combination. As a result, the total number of samples is $101 \times 81 \times 41 \times 41 = 13752261$.

For the purpose of the present study, the state space of parameters is then further divided into six subsets. Primarily, this division is carried out to attain reasonable processing and training times for the developed MCNN models. Secondly, qualitative conclusions can be drawn later through a comparison of individual models. The division is carried out only in terms of A and Δh^*. The underlying matrix of 1681 x and β combinations corresponding to each A+Δh^* combination is left unchanged. In particular, the overall A-Δh^* state space is divided into: upper-left (LU), upper-right (RU), bottom-left (LB) and bottom-right (RB) corner, center (C) and grid (G) subsets – see Fig. 2. Each of the zoomed-in subsets (LU, RU, LB, RB & C; see Fig. 2) contains $11 \times 11 = 121$ A+Δh^* combinations. The grid subset (G; green points in Fig. 2) contains $8 \times 10 = 80$ A+Δh^* combinations evenly spread across the main state space. The exact A+Δh^* combinations are, for all subsets, tabulated in the supplementary online material. Each of these subsets will be used for the training of an individual MCNN model. The corners of the overall state space are chosen as subsets so that the performance of the MCNN models can be evaluated in the borderline/extreme (temperature-wise) cases of the potentially encountered glass transition behavior, with the corresponding temperature ranges being characteristic for the polymers (low-T data) and oxide glasses (high-T data). The center subset represents a temperature range typical for the chalcogenide or fluoride glasses. Whereas these zoomed-in subsets (LU, RU, LB, RB & C; see Fig. 2) contain structural relaxation data from rather narrow temperature regions, the opposite is true for the grid (G) subset, which tests the MCNN models' ability to fully comprise the whole T_g-relevant temperature scale. Note that the G subset still works with only a small subset of the A+Δh^* combinations. The visualization of the temperature ranges relevant to each of the subsets is included in the supplementary online material. By assessing the performance of MCNN models acquired on these subsets, we can reasonably assume acceptable accuracy of estimates across the entire matrix of simulated A, Δh^*, x, and β combinations.

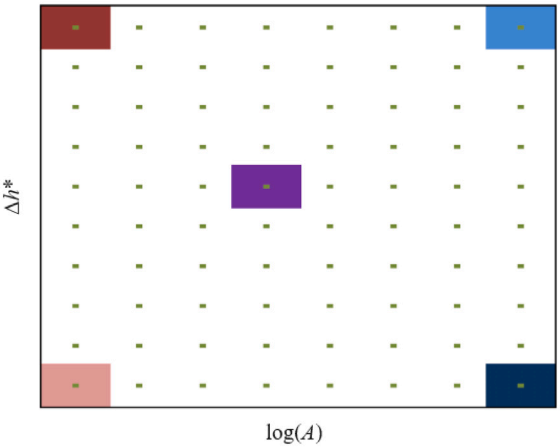

Fig. 2. Overall state space of A, Δh^* combinations and colored sub-spaces used for training individual models: upper-left (LU), upper-right (RU), bottom-left (LB), and bottom-right (RB) corner, center (C) and grid (G). For a scale reference: each green rectangular dot represents one A, Δh^* combination.

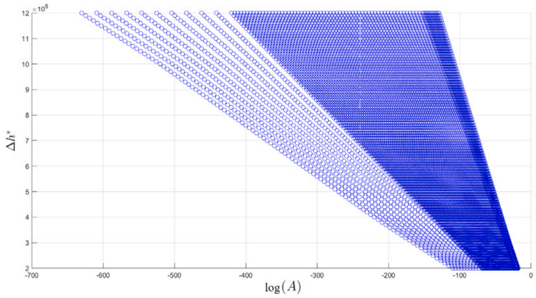

Fig. 3. State space of A and Δh^* parameters.

2.2. Multi-scale neural model

One of the prominent advantages intrinsic to multi-scale neural networks resides in their capacity to efficiently accommodate signals exhibiting varying frequency characteristics. Through the integration of multiple layers of processing, each tailored to disparate scales, multi-scale networks demonstrate the adeptness to comprehensively apprehend both the low-frequency and high-frequency constituents of a signal. This inherent capability renders them eminently suitable for a diverse array of applications spanning audio and speech processing, as well as image and video analysis [54].

Recent investigations have introduced pioneering multi-scale architectural paradigms, featuring the integration of attention mechanisms [55], recurrent connections [56], and unsupervised learning [57]. These innovative approaches have exhibited promising outcomes in various tasks, including speech enhancement, image restoration, and anomaly detection.

In this study, an innovative multi-scale neural model architecture for extracting TNM model parameters (A, Δh^*, x, and β) from relaxation signals is proposed. The architecture is composed of three sequential modules: a preprocessing module, an extraction module, and a fully-connected module.

The preprocessing module is responsible for preparing the input data by analyzing the six distinct relaxation signals. It applies a multi-scale approach to examine the data across different frequency components, ensuring that relevant features are preserved while reducing computational complexity. This module also identifies significant segments of the input signals–those sections that are most relevant for the task of parameter estimation–allowing the network to focus its

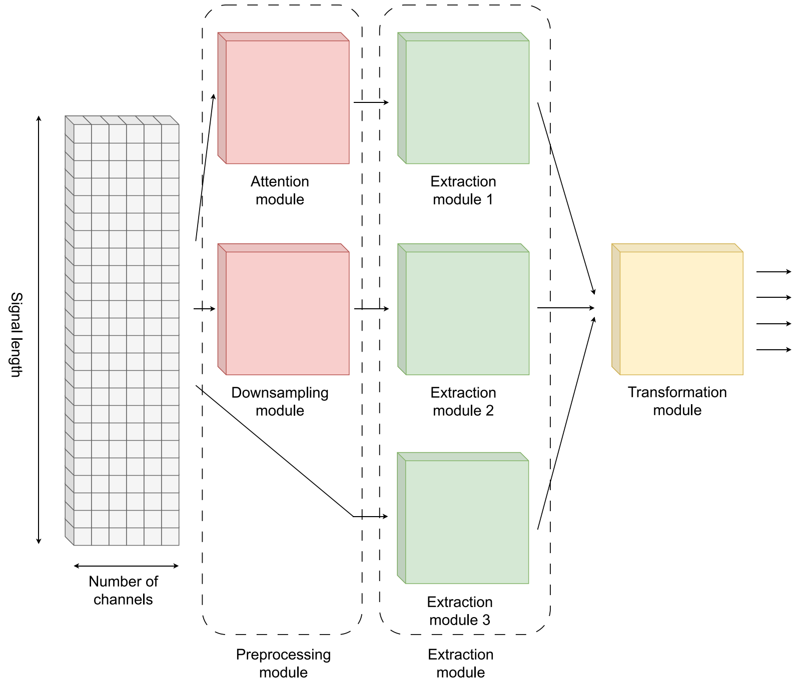

Fig. 4. Overall architecture of the presented implementation of a multi-scale convolutional neural model. In the model, a series of six relaxation signals of constant length serves as the input. Based on this input, the model provides TNM model parameter estimates A, Δh^*, x, and β.

attention on key parts of the data. By isolating these segments, the preprocessing module ensures efficient data handling and improves the accuracy of feature extraction in subsequent stages.

The extraction module performs multi-scale feature extraction by applying a series of convolutional operations to the pre-processed signals. This module is designed to capture meaningful patterns within the data at multiple temporal resolutions, from fine details to broader trends. By using parallel branches with varying receptive fields, the extraction module is able to process the input at different scales, enabling the model to learn both local and global structures inherent to the relaxation dynamics. The hierarchical structure of this module allows the network to progressively refine the features extracted from the input signals, which are essential for the subsequent prediction of model parameters.

The fully-connected module serves as the final stage of the architecture, where the features extracted by the convolutional layers are transformed into the desired output. This module combines the information from multiple feature maps and applies a series of dense layers to learn complex interactions between the extracted features. It ultimately produces the quartet of output values corresponding to the A, Δh^*, x, and β parameters. The fully-connected module integrates the multi-scale features in a way that facilitates accurate and robust predictions, ensuring that the final output reflects the intricate dependencies observed in the input data.

The overall architecture of the proposed neural model is depicted in Fig. 4.

2.2.1. *Preprocessing module*

The objective of this module encompasses two primary functions: the downsampling module and the attention module. The downsampling module involves downsampling the input signal (relaxation signal) to a different sampling period, thereby ensuring a multi-scale approach to the entire input data processing. If the input signal $C_\mathrm{p}^\mathrm{N}(T)$ is given by n discrete values for equidistant temperature points $T_0, T_1, \ldots, T_n$, the downsampled signal $C_\mathrm{p}^{\mathrm{N}\prime}(T')$ is determined by the following formula.

$$C_\mathrm{p}^{\mathrm{N}\prime}(T') = C_\mathrm{p}^\mathrm{N}(k_\mathrm{down}T), \tag{6}$$

where $k_\mathrm{down} > 1$ is the integer value of the downsampling coefficient and $T' = 0, 1, \ldots, \frac{n}{k_\mathrm{down}}$. Another module – the attention module – is tasked with identification of a significant segment within the relaxation signal and forwarding this segment for further processing. A significant segment is referred to as an interval during which the signal exhibits marked non-constancy. It is worth noting that the length of these significant segments varies considerably, and for some samples, may correspond to only a few discrete points. Hence, the significant segment needs to be interpolated in order to provide an adequate amount of data representing the shape of the curve's peak.

For the purposes of the data preprocessing, the significant segment of the signal C_p^N is defined as the sequence C_p^N (T_sig), $T_\mathrm{sig} = T_i, T_{i+1}, \ldots, T_j$. T_i is the temperature, for which $0 < C_\mathrm{p}^\mathrm{N}(T_i) < \epsilon$, and $\frac{\mathrm{d}C_\mathrm{p}^\mathrm{N}(T)}{\mathrm{d}T}|_{T=T_i} > 0$. T_i is the temperature, for which $1 - \epsilon < C_\mathrm{p}^\mathrm{N}(T_i) < 1$ and $\frac{\mathrm{d}C_\mathrm{p}^\mathrm{N}(T)}{\mathrm{d}T}|_{T=T_j} < 0$, where $\epsilon > 0$ is small real value. In order to normalize the length of the significant segment, the sequence C_p^N (T_sig) is interpolated by an m-degree polynomial $P(T) = \sum_{k=0}^{m} \alpha_k T^k$ such that the following holds.

$$\sum_{T=T_i}^{T_j} \left[C_\mathrm{p}^\mathrm{N}(T) - P(T)\right]^2 \rightarrow \min. \tag{7}$$

The polynomial $P(T)$ is employed to determine interpolated n_interp values $C_\mathrm{p}^\mathrm{N}(T_\mathrm{interp})$ for T_interp equidistantly spread on interval $\left[T_i; T_j\right]$. A visualization of all steps executed within the attention module is presented in Fig. 5.

The selection of parameter values was determined through a balanced blend of prior domain expertise and preliminary experiments as follows: The downsampling coefficient $k_\mathrm{down} = 3$; the degree of interpolating polynomial $P(T) = 3$; the number of interpolated values $n_\mathrm{interp} = 1000$.

2.2.2. *Extraction module*

In the extraction module, it is advisable to employ a sequence of convolutional and max-pooling layers for feature extraction from the input signal, as the combination of these layers is effective in capturing

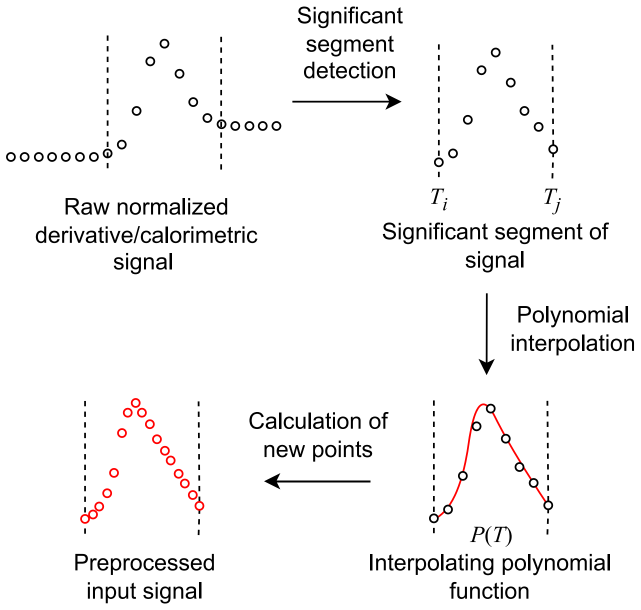

Fig. 5. All steps executed in the attention module.

hierarchical patterns and reducing spatial dimensions, enabling the neural model to discern relevant features efficiently.

In the proposed neural model, three parallel feature extraction modules are incorporated. The initial module extracts features from the data received from the attention module during the preprocessing stage. The second module processes the signal obtained from the downsampling module. Finally, the third module is supplied with the original set of relaxation signals.

In all three extraction modules, the architecture follows an identical structure, differing only in the kernel sizes of the convolutional layers. The choice of varying kernel sizes allows the network to capture features at multiple temporal resolutions, which is crucial for modeling the complex multi-scale nature of the input signals. Initially, the six input signals are split into individual channels, with each channel processed independently to retain the unique characteristics of each signal. This independent processing enables the model to learn distinct patterns from each signal while preserving their individual temporal dynamics.

Each channel is then passed through a 1D convolutional layer, followed by a max-pooling layer to reduce the dimensionality and emphasize the most relevant features. This combination of convolution and pooling is repeated twice more, creating a hierarchical structure that progressively extracts higher-level features from the data. The ReLU activation function is used in every convolutional layer, as it introduces non-linearity into the model and enhances its ability to learn complex dependencies within the data. The use of max-pooling layers ensures that the model reduces redundant information, focusing on the most salient aspects of the input signals.

After the convolution and pooling operations, a fully connected layer with a hyperbolic tangent $(\tanh)$ activation function is employed. The $\tanh$ function is chosen for its ability to map the extracted features to a continuous range, enabling the model to learn more nuanced relationships between the features. This layer enhances the model's expressiveness by allowing it to capture subtle variations in the data, which are critical for accurate parameter estimation.

To further promote robust training and mitigate overfitting, a dropout layer is applied at the end of each extraction branch. This regularization technique prevents the model from becoming overly dependent on specific neurons, thereby improving its generalization ability. The dropout layer introduces stochasticity into the training process, ensuring that the model can learn representations that are more resilient to variations in the input data.

The kernel sizes used in the convolutional layers vary across the three extraction modules, with sizes of 4, 12, and 24 in the first, second, and third modules, respectively. This design allows the model to capture both fine-grained details and broader temporal patterns. Smaller kernels focus on localized features in the input signals, while larger kernels detect more global patterns. The use of varying kernel sizes ensures that the network can effectively model both short-term and long-term dependencies in the relaxation dynamics. The overall architecture of the extraction module is depicted in Fig. 6.

2.2.3. Transformation module

The transformation module, which is integrated at the end of the proposed neural model, assumes a essential role in the data processing pipeline. This allows the model to transform prominent features extracted using prior modules into the desired quartet of values A, Δh^*, x, and β.

The architecture of the transformation module is designed to efficiently process and transform the incoming signals from preceding modules. First, a concatenation layer is employed to merge three signals from the previous modules. This concatenation step enables the model to fuse essential feature representations from multiple sources, enhancing the overall information flow.

Subsequently, the signal undergoes a series of transformations through two consecutive fully-connected layers (32 neurons), each equipped with hyperbolic tangent $(\tanh)$ activation functions. These layers are strategically positioned to capture and model the intricate relationships among the concatenated features, allowing the network to learn complex patterns and abstractions within the data. In order to produce the desired quartet of output parameters, an output layer with four neurons is connected at the end of the module. Each neuron corresponds to one of the output parameters, and a linear activation function is applied. The chosen linear activation function ensures that the module outputs a linear combination of the learned features, resulting in the four A, Δh^*, x, and β output values. The architecture of the transformation module is shown in Fig. 7.

2.3. Training strategy

In the pursuit of optimizing the performance and robustness of the proposed neural model, the development of an effective training strategy is of prime importance. The central emphasis of the training process is navigating the intricacies of managing large-scale datasets, making it inherently intertwined with the nuances of big data processing.

The overall state space of data was sub-divided into 6 smaller subsets, as it was thoroughly covered in Section 2.1. To accommodate the substantial size of these datasets, significant hardware and software optimizations were necessary to ensure the efficiency of the data retrieval process. Each dataset is then shuffled and separation is done in $70, 15, 15$ % ratio to obtain training, validation, and testing set, respectively.

Input consists of signals with dimensions 6×18501, output is a corresponding quartet of 4×1 parameters: A, Δh^*, x, and β. This is contrary to the dataset acquisition process, wherein the input comprised of the mentioned quartet of TNM parameters, for which six signals were calculated. Input signals are processed via the aforementioned pre-processing module in the input layer of the ANN.

Prior to inputting the target into the ANN, it is essential to perform normalization, restricting the values to the interval $[0, 1]$. The process of normalizing target data is done based on Min–max feature scaling. Min–max normalization scales data points to a range of $[0, 1]$, where 0 represents the minimum and 1 represents the maximum values in the dataset. Given a target vector y with minimum values a and maximum values b, the Min–max normalization of target vector is calculated as

$$y_{\mathrm{n}}(k) = \frac{y(k) - a(k)}{b(k) - a(k)}, \tag{8}$$

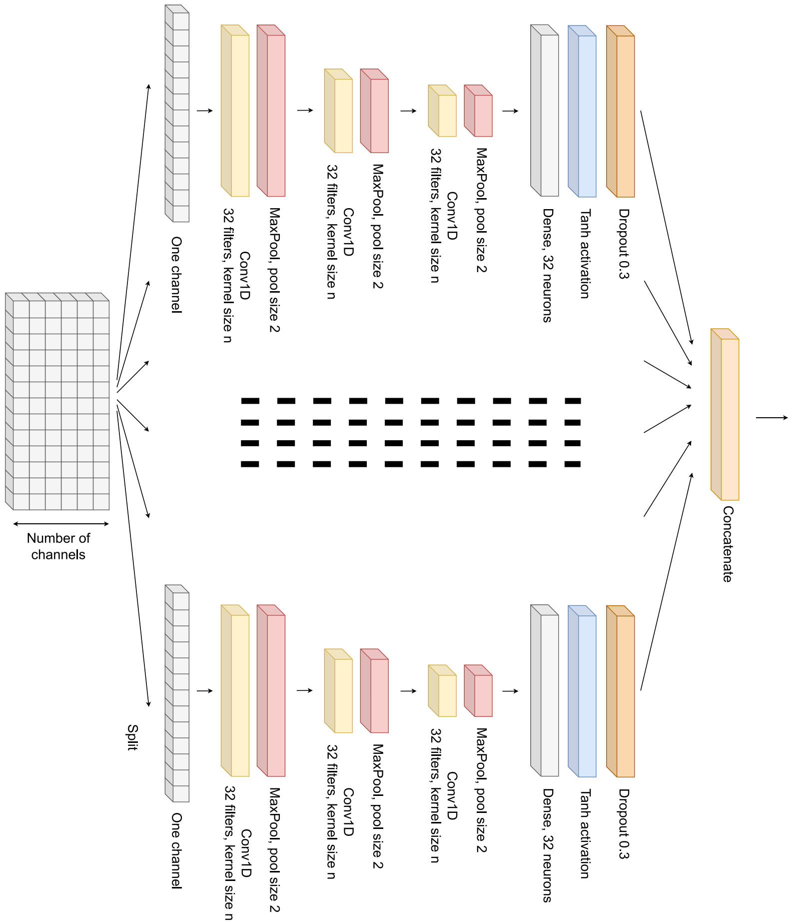

Fig. 6. Extraction modules 1-3. Input multi-channel signal is split into six separate branches, each of them processed individually.

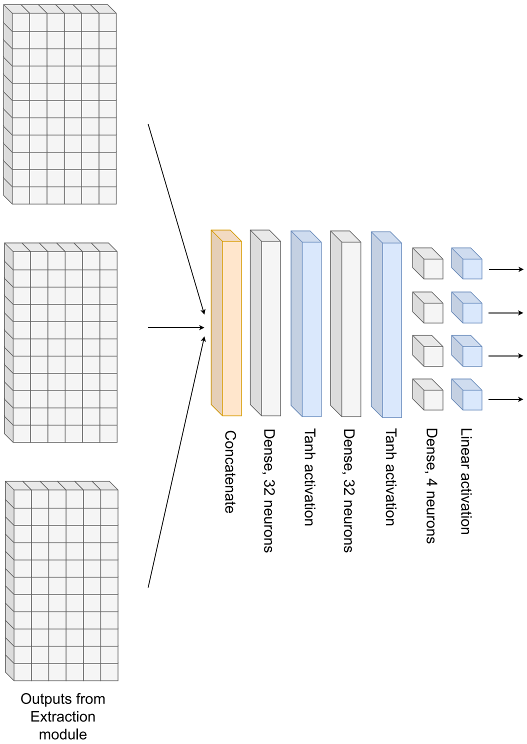

Fig. 7. Transformation module: the output layer directly provides the TNM model parameters of interest$A$, Δh^{*}, x, and β.

Table 3
Lower & upper Min–max normalization limits.

y	Lower limit	Upper limit
Δh^{*}	$2 \times 10^{5}/1.2$	$12 \times 10^{5} \times 1.2$
$\log(A)$	$-630/1.2$	-18.4×1.2
β	$0.2/1.2$	1.0×1.2
x	$0.2/1.2$	1.0×1.2

where $k = 1, \dots, 4$. To obtain physically meaningful values at the output of the ANN, the output values must be denormalised as

$$y(k) = y_{\mathrm{n}}(k)(b(k) - a(k)) + a(k).$$

Minimum and maximum values are based on limit values of the overall dataset of parameters with added reserve and are summarized in Table 3.

Min–max normalization preserves relative relationships between data points, proving beneficial for algorithms sensitive to feature scales, like gradient-based optimization algorithms in machine learning.

To calculate the error for a given normalized target-predicted output pair, the following approach was applied, where the values are indexed as $k = 1, \dots, 4$. This is achieved in the loss function. Firstly, a squared difference vector is obtained as

$$\Delta^{2} y_{\mathrm{n}}(k) = y_{\mathrm{n,true}}(k) - y_{\mathrm{n,pred}}(k). \tag{9}$$

Subsequently, each value in the squared difference vector is weighted by the corresponding weight from the weights vector, resulting in a weighted squared difference vector

$$\Delta^{2} y_{\mathrm{wn}}(k) = \Delta^{2} y_{\mathrm{n}}(k) w(k), \tag{10}$$

The final error value is obtained as reduced mean of weighted squared difference vector

$$\bar{x}_{\mathrm{R}} = \frac{1}{4}\sum_{k=1}^{k=4} \Delta^2 y_{\mathrm{wn}}(k). \tag{11}$$

Given that individual parameters have distinct impacts on the output signal, the selection of the weights vector w in Eq. (10) is of utmost importance and is a result of thorough, iterative observations that determined values $w = [1.0, 1.5, 3.0, 3.0]$ for: A, Δh^*, x, and β respectively. The firstly trained models exhibited great accuracy in resulting predicted-target signal shape, a common pattern was observed in which the predicted output signal mainly shifted along the temperature x axis. This phoenomenon was explained in estimation error of $\log(A)$ parameter. As a result, the decision was made to reinitiate the training process, setting the $\log(A)$ weight to $w_{\log(\mathrm{A})} = 0.1$. This adjustment aimed to alleviate the sensitivity with which the ANN learns to estimate the $\log(A)$ parameter. This change was carried out mainly because the $\log(A)$ value can later be easily determined by alternative fitting approaches. Therefore the final weights for A, Δh^*, x, and β are selected as follows.

$$w = [1.0, 0.1, 3.0, 3.0]. \tag{12}$$

A total of 7 models have been acquired and are detailed in this section, including their distinctive training process features. To recapitulate: the Dataset creation section discussed creation of several datasets from the overall state-space of parameters. Originally, there were 5 datasets defined: upper-left, upper-right, bottom-left and bottom-right corners and central part of the overall dataset. For each of these datasets, an individual model was trained. Upon evaluation of these models, a need to observe an impact of $w_{\log(\mathrm{A})}$ on the quality of models has arisen, as well as a need to make general conclusions on patterns occuring in the studied phenomena. Hence, two additional control models, designated as the 6th and 7th models, were acquired. For purposes of training a 6th model, a new dataset was designed: grid dataset, which sparsely spans across the entire state space of parameters (see Fig. 2). Additionally, a 7th control model was obtained for central dataset with its own unique value of $w_{\log(\mathrm{A})} = 1.0$.

The Stochastic Gradient Descent (SGD) algorithm was selected as the optimizer for the MCNN model training. This choice is based on the algorithm's well-established performance in a wide range of machine learning tasks, particularly for its ability to efficiently handle large-scale datasets. One of the primary reasons for SGD selecting is its simplicity and scalability, which allows for the processing of vast amounts of data without excessive computational overhead. Moreover, SGD's inherent stochastic nature enables the model to escape local minima more effectively than batch gradient methods, thereby improving generalization capability across diverse datasets [58]. Given the complexity and size of the training dataset in this study, SGD provides an optimal balance between convergence speed and memory efficiency.

Reduced mean square error (Eq. (11)) was used to evaluate the training process and the mean absolute error function is applied to validate the results.

All parameters used in the training process, including learning rate, batch size, and stopping criteria, are summarized in Table 4, providing a comprehensive overview of the selected hyperparameters. These choices were guided by extensive experimentation to optimize both training time and model performance, ensuring that the MCNN converges efficiently while maintaining high accuracy.

Table 4
Parameters of training.

Input shape	18501 × 6
Training algorithm	SGD algorithm
Loss function	Reduced mean square error
Validation metric	Mean absolute error
Maximum epochs	200
Stopping criterion	Maximum epochs reached
Learning rate α	0.01
Batch size	128

3. Results and discussion

The present section will be split into four parts. First, the evaluation metrics for the assessment of the MCNN models' performance will be introduced. Second, the quality of the MCNN models' estimates of the TNM parameters will be evaluated based on the magnitude of the estimates errors. Third, more complex evaluation metrics seeking the correlations between the performance of the individual MCNN models and the particular types of structural relaxation behavior will be discussed. Fourth, more general conclusions about the overall performance of the current MCNN models in relation to their usability for real-life data evaluation will be drawn.

3.1. Evaluation metrics

The performance of the individual MCNN models was assessed based on the following metrics. The two fundamental criteria were the absolute errors (AE in figures) and the sum of squared errors (SSE). Absolute error metric (Eq. (13)) is used only for individual TNM parameters (A, Δh^*, x, and β). On the other hand, SSE is calculated for both the TNM parameters (A, Δh^*, x, and β, see Eq. (14)), and the relaxation signals (see Eq. (15)), where relaxation signals are a set of six CHR heating steps in the $C_{\mathrm{p}}^{\mathrm{N}}$ form.

$$AE = \left| P_{\mathrm{true}} - P_{\mathrm{pred}} \right|, \tag{13}$$

where P is a scalar value of a given TNM model parameter.

$$SSE_{\mathrm{P}} = \sum_{i=1}^{2 \text{ or } 4} \left[P_{\mathrm{true}}(i) - P_{\mathrm{pred}}(i) \right]^2, \tag{14}$$

$$SSE_{C_{\mathrm{p}}^{\mathrm{N}}} = \sum_{T_i=T_{min}}^{T_{max}} \left[C^{\mathrm{N}}_{\mathrm{p\ true}}(T_i) - C^{\mathrm{N}}_{\mathrm{p\ pred}}(T_i) \right]^2. \tag{15}$$

In their raw form, these metrics were calculated for each sample from the test subset and plotted in ascending order for each individual MCNN model – an example of such visualization is shown in Fig. 9a, 9b. It is important to note that the input samples with the values of $C_{\mathrm{p}}^{\max} > 6$ (where $C_{\mathrm{p}}^{\max}$ is the $C_{\mathrm{p}}^{\mathrm{N}}$ value reached in the maximum of the relaxation peak as shown in Fig. 8e) were omitted from the evaluations because such relaxation signals are very rare in real-life materials, and the SSE metrics would be arbitrarily distorted due to the extreme statistical weights of these samples. To further compare the performance of the individual networks, the particular absolute error and SSE metrics were plotted individually, with all profiles corresponding to the individual MCNN models being combined – example of such visualization is shown in Fig. 8ac. As the evaluation for each MCNN model covered a slightly different number of tested samples (due to the different percentage of $C_{\mathrm{p}}^{\max} > 6$ cases being involved and omitted), the evolution of the absolute error and SSE profiles was compared with dependence on the number of samples expressed as percent of each individual total amount (corresponding to the given MCNN model). Apart from the metrics being simply arranged in ascending order, they were also plotted depend on several analytical quantities characterizing the $C_{\mathrm{p}}^{\mathrm{N}}$ curves to reveal the potential correlation between the shape of the relaxation signal and the performance of the MCNN models. The employed analytical quantities were: $C_{\mathrm{p}}^{\max}$, ΔT^{hw} and $C_{\mathrm{p}}^{\max}/\Delta T^{\mathrm{hw}}$, where ΔT^{hw} is defined as the difference between the temperatures corresponding to the maximum of the relaxation peak and first cross-section of the experimental data with the extrapolated $C_{\mathrm{pl}}(T)$ line – see Fig. 8e for the corresponding visualization.

In order to identify the mutual correlations between the accuracies of MCNN-based estimates of individual TNM parameters, the evaluation metrics were plotted in a 3D space as dependencies of selected

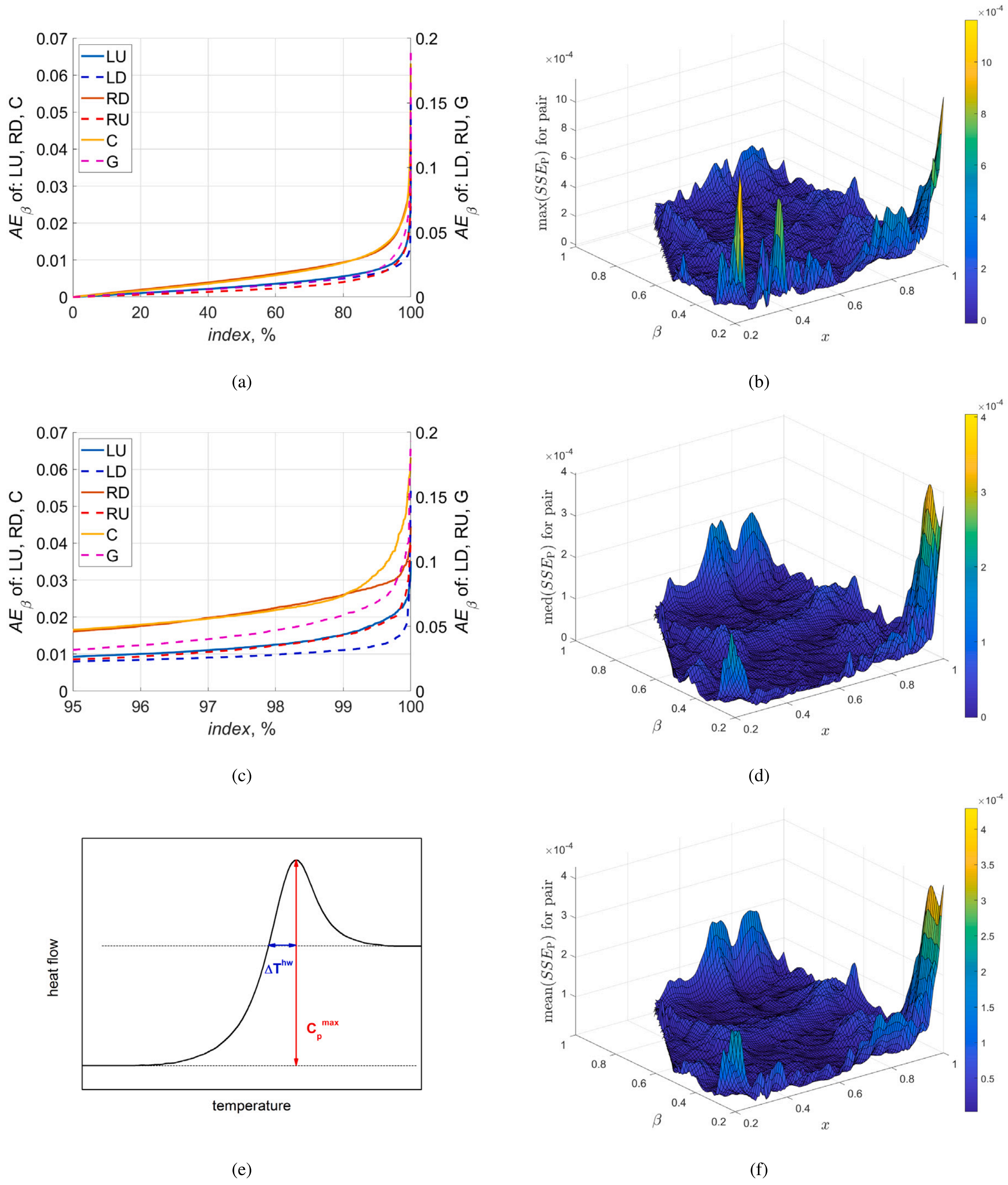

(a)

(b)

(c)

(d)

(e)

(f)

Fig. 8. Sorted absolute β error across all models (a) and its detail (c). Pair of basic analytical quantities of relaxation peak (e). Comparison of various statistical representations of LU model's SSE, calculated for parameters present on (x, y) axis (bdf).

pairs of the TNM parameters – see Fig. 8bdf for an example of such depiction. Whereas the signals SSE metric (Eq. (15)) was plotted in an identical form (as determined by Eq. (13)), an SSE metric for the TNM parameters (Eq. (14)) could not be used due to the different error scales (corresponding to the nominal absolute magnitudes) of the individual TNM parameters (see Table 2). Therefore, the parameters SSE were calculated based on the normalized values of these parameters. An identical normalization such as that used during the training of the MCNN models (see Eq. (8)) was applied. The SSE of the TNM parameters (Eq. (14)) was calculated in two variants: either for all four TNM parameters or for the two parameters present on the X and Y axes (see Eq. (14)) of the given 3D plot. As a further consequence, both the SSE of C_p^N and the SSE of A, Δh^*, x, and β (represented by a wide distribution of errors in the 2D graphs, see e.g. Fig. 9a, 9b) had to be represented by a single value, which was then attributed to the given pair of the TNM parameters. By considering the maximum, median, and mean values, the mean representation was found to best reflect all features of the given 3D spaces of the error metrics – see Fig. 8bdf.

3.2. Absolute errors

The performance of the trained MCNN models can be best evaluated based on the magnitude of the absolute errors provided by the individual TNM parameter estimates: A, Δh^*, x, and β (see Eq. (13)). In other words: for each single parameter, a corresponding absolute error is obtained. Very good results were obtained for the parameters β and x, which are primarily responsible for the height and width of the relaxation peak (and, therefore, ideally expressed by the CHR cycles set). Starting with the non-exponentiality parameter β (see Fig. 9c), 90% of all MCNN-based estimates are well below the ± 0.02 error level, which could be considered the top methodological performance of the alternative non-fitting approach, which is the simulation-comparative method based on the comparison of the theoretically simulated and experimentally measured C_p^{max} values during the CHR cycles. Moreover, only approx. 2% of the estimates obtained for the G subset and < 1 % of the estimates obtained for the RU subset exhibit errors larger than ±0.05 (see the zoomed-in inset in Fig. 9c). Note that the ±0.05 errors in β can be considered a benchmark for the curve-fitting determination of this parameter due to the irreproducibility and distortions in the real-life data. In addition, the change of β by 0.05 can also be considered the first significant and interpretable variation of the non-exponential behavior with regard to e.g. compositional or structural trends in real-life materials. Whereas the worse performance of the MCNN trained for the G subset is understandable (the neural network had to interpolate through larger state space while being trained with fewer representatives for each typological structural relaxation behavior), the significantly worse performance in the case of the RU subset is quite interesting. Since this subset includes rather rare high-T data with very broad relaxation peaks (characterized by low values of Δh^* and A), the MCNN needs to distinguish between small relaxation signal nuances (differentiated in the Y coordinate) along the range of more than 400 °C – see Fig. S1 in the supplementary online material. The apparent issue with the recognition of very broad relaxation signals (C_p^N) is worth bearing in mind for later discussion. Nonetheless, any β estimates with absolute error ≤ 0.1 are still very much usable in the base characterization of the material's class and for the categorization of its structural relaxation behavior.

Even better performance of the trained MCNN models was observed in the case of the estimates of the TNM parameter of non-linearity x – see Fig. 9e. Here, over 99 % of all estimates had absolute error < 0.02; the only exception was the training and testing of the G subset, where "only" 97% of the estimates fell below this mark. The performance of the MCNN is, in the case of the x estimates, better or at least comparable to the estimates provided by the alternative non-fitting approach: the simulation-comparative method [59]. However, even for the G subset, the remaining ~3% of estimates were still obtained with absolute error < 0.05, which is on par with the second non-fitting method aimed at the determination of the non-linearity parameter x, the peak-shift method [60]. Similarly to the β estimates, this level of accuracy is more than sufficient for all interpretations of compositional trends in the structural relaxation behavior of real-life materials. The MCNN-based estimates of the parameter x are also much less dependent on the shape of the particular relaxation peaks, as evidenced by the significantly lower variation of the absolute error among the individual MCNN models (developed for the given subsets).

Contrary to the shape-defining TNM parameters (β and x), the position-defining parameters (Δh^* and A) were estimated with a lot more substantial absolute error. For Δh^*, the typical errors of the most precise and robust non-fitting method [61] are ~10 $\mathrm{kJ\,mol^{-1}}$; this benchmark was in case of absolute majority of the MCNN models achieved only for approx. 20% of estimates – see Fig. 9d. Interestingly, the RU subset (for which significantly higher absolute errors were obtained for the estimation of β) was found to be quite suitable for the determination of Δh^*, and the 10 $\mathrm{kJ\,mol^{-1}}$ benchmark was fulfilled for 70 % of the estimates. As the apparent activation energy influences (apart from the position of the relaxation peak on the temperature axis) the width of the relaxation peak, the significantly broader C_p^N signals obtained within the RU state space evidently provide better X-axis data resolution for the MCNN to recognize and attribute the correct Δh^* value – see Fig. S1 in the supplementary online material. Considering the typical compositional trends observed for the enthalpy relaxation data, absolute errors above ~ 50 $\mathrm{kJ\,mol^{-1}}$ should be considered unacceptable even for the base categorization of the class and relaxation behavior of the materials with low-T glass transition. Owing to the scaling manifestation of the Δh^* parameter, its absolute error decreases in importance as Δh^* increases. As the RU subset corresponds to the low Δh^* and A values, the negative impact of Δh^* absolute errors is partially compensated in combination with low absolute $\log(A)$ values. Hence, at high temperatures (low absolute $\log(A)$ values), the absolute errors obtained for the MCNN estimates can be assumed acceptable across the whole Δh^* range. As the temperature of the glass transition decreases, the errors associated with the estimates by the present MCNN architectures significantly increase. The consequences of this finding will be further discussed in Section 3.4. Apart from the other subsets for corners and center of the overall state space zoomed-in subsets (LU, RU, LB, RB & C; see Fig. 2), a further decrease in the accuracy of the MCNN-based estimates was observed for the overreaching G subset. Since this subset model is currently the closest approximation of the potential universal neural network, the via-training obtained MCNN models (in their present form) would not be suitable for the determination of the Δh^* parameter.

From the practical point of view, the worst performance of the MCNN-based estimates was observed in the case of the A determination – see Fig. 9f (note that the absolute error are calculated for the pre-exponential factor in the form of $\log(A)$). The severity of the absolute errors magnitude can be judged based on the variation span of the $\log(A)$ values contained in each state space subset. For example, the central (C) subset includes a maximum variation of $\Delta \log(A) \approx 25$, which is reflected in approx. 70 °C difference in the position of T_g – see Fig. S2 in the supplementary online material. For a majority of low-to-middle temperature applications ($T < 400$ °C), the minimum acceptable accuracy of the T_g determination is somewhere around ±5 °C. This would translate into the maximum $\log(A)$ absolute error of $\sim 1-2$. As can be seen in Fig. 9f, such accuracy of the MCNN estimates is barely achieved for $10-20$ % of samples. Somewhat better performance was (due to the scaling) achieved in the case of the LD subset estimates, where the maximum variation of $\Delta \log(A) \approx 200$, which is reflected in approx. 115 °C difference. In this case, the $\log(A)$ absolute error of ~ 8–10 (corresponding to $\Delta T_g \approx \pm 5$ °C) is achieved for approx. 50 % of all LD subset estimates. Nonetheless, the MCNN estimates of the $\log(A)$ value can be, in general, considered unreliable in the present state, which was most probably caused by the low $\log(A)$ weight during the MCNN training.

3.3. 3D-plotted SSE metrics

In order to check the potential correlation between the performance of the particular MCNN models and the shape of the relaxation peaks, the absolute errors were plotted with dependence on the analytical quantities (C_p^{max}, ΔT^{hw}, and $C_p^{max}/\Delta T^{hw}$; see Fig. 8e). Interestingly, no direct correlations between any absolute error profile (obtained for different combinations of TNM parameters and state space subsets) and the analytical quantities were found. This indicates that more complex relations between the particular absolute error profiles and archetypal relaxation behaviors need to be sought. Hence, the SSE metrics for either signals (Eq. (15)) or pairs/quartets of TNM parameters (Eq. (14)) were plotted in a 3D space as dependencies of selected pairs of the TNM parameters (see Section 3.1 for the evaluation details). In this regard, four pairs of potentially correlating TNM parameters were selected: Δh^* & $\log(A)$, Δh^* & x, Δh^* & β, x&β. By careful examination of the SSE profiles of the individual subsets (LU, RU, LB, RB, C & G; see Fig. 2), it was found that all trends observed within these subsets are sufficiently well represented by the overarching G subset, which covers the whole Δh^*-$\log(A)$ state space, although with lower resolution.

Additionally, the primary distinction observed across all model comparisons was related to the MCNN's performance. Specifically, the accuracy of the MCNN's estimates deteriorated at the boundaries

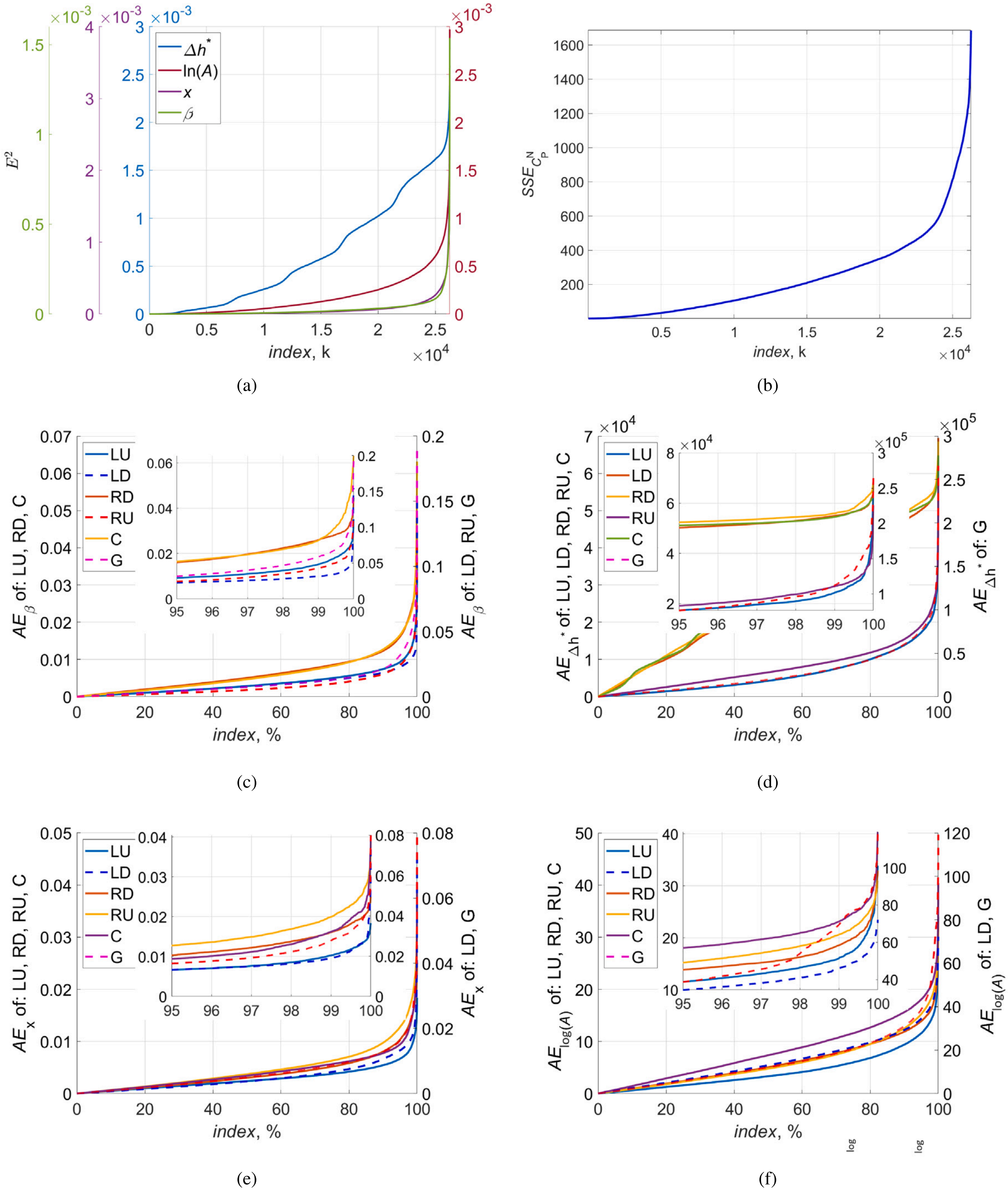

(a) (b) (c) (d) (e) (f)

Fig. 9. Sorted absolute error for each parameter of central (C) model (a), sorted $SSE_{C_p^N}$ for true and predicted signal of C model (b). Sorted absolute errors for a given parameter across all models: β (c), Δh^*(d), x (e), $\log(A)$ (f).

of the cutout subsets within the overall state space. This decline in accuracy was attributed to the limited capacity of the MCNN to perform interpolation in these edge regions.

These state space areas with increased errors are thus just an artifact of the cutout procedure, artificially distorting the potential dependences of SSE on particular TNM parameters. For these two reasons, only the results for the overarching G subset will be shown and discussed. On the contrary, as was already mentioned in Section 3.1, three types of metrics will be displayed for each combination of the TNM parameters on (x, y) axis: SSE for signals, SSE for all four parameters, and SSE for the displayed pair of TNM parameters (see z axis label on Fig. 10ace, for example).

The dependencies of the SSE metrics on the Δh^* & $\log(A)$ combination of the TNM parameters are shown in Fig. 10ace. The evolution of the SSEs for signals (Fig. 10a) is a direct consequence of the comparatively broader temperature ranges across which the glass transition evolves (as depicted in Fig. S1 in the supplementary online material). The broader the range, the larger number of data-points is influenced by any unideality (incorrect estimate), and thus the higher impact on the overall SSE. The close resemblance of the SSE profiles for the TNM parameters quartet and pair indicate that Δh^* and/or $\log(A)$ has significantly larger impact on the overall SSE, that is computed via Eq. (14) for two or all A, Δh^*, x, and β parameters that are firstly normalized using Eq. (8). Despite this fact, it is these two TNM parameters (Δh^* & $\log(A)$) that were determined with the highest absolute error by the

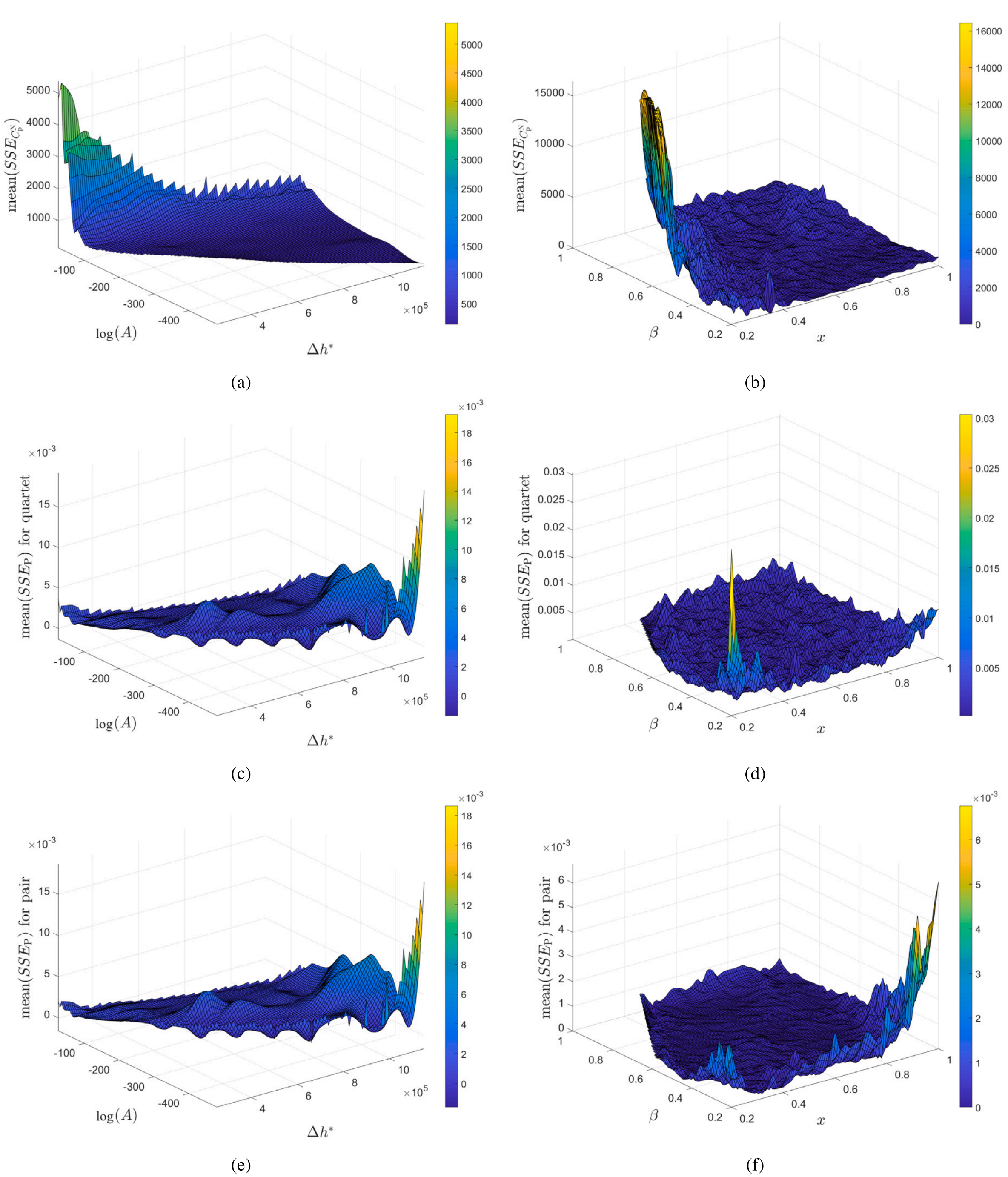

(a) (b) (c) (d) (e) (f)

Fig. 10. G model dependencies on SSE metrics (Eqs. (14) & (15)): $(\Delta h^*, \log(A), SSE)$ (ace); (x, β, SSE) (bdf).

MCNN. Regarding the factual shape of the SSE hyperspace, the most extreme cases of structural relaxation behavior (very broad transitions in RU region, and the very narrow transitions in the LD region) seem to be the most difficult to be accurately comprehended by the MCNN from the positional point of view; a view for which the Δh^* & $\log(A)$ combination is responsible.

The TNM parameters responsible for the shape of the relaxation peak – the x&β combination (see Fig. 10bdf for the corresponding SSEs) – were determined by all MCNN models quite accurately. The relatively high scatter (the bottom surface is not flat, but rather irregular/uneven / rippled) of the signals SSE hyperspace (see Fig. 10b) confirms the secondary role of these two parameters on the overall SSE of the signals. The natural explanation of the hyperspace shape can be attributed to the decrease of C_p^{max} with high x and low β. The corresponding deviations/errors then propagate proportionally to the height of the structural relaxation peak. The discrepancy – which is approx. one order of magnitude – between the SSE's of the parameters quartet and pair (see Fig. 10df) confirms that the normalization expressed by Eq. (8), and calculation expressed by Eq. (14), favors (gives higher impact to) the Δh^* & $\log(A)$ quantities. Regarding the factual shape of the SSE hyperspace depicted in Fig. 10f: the two parameters are estimated with extreme accuracy across an absolute majority of the relaxation behavior archetypes (the SSE surface forms a flat bottom). The only region with increased inaccuracy of the estimates is the case of the relaxation peaks with lowest C_p^{max} (high x and low β), where the extreme similarity of the relaxation signals with large changes of either

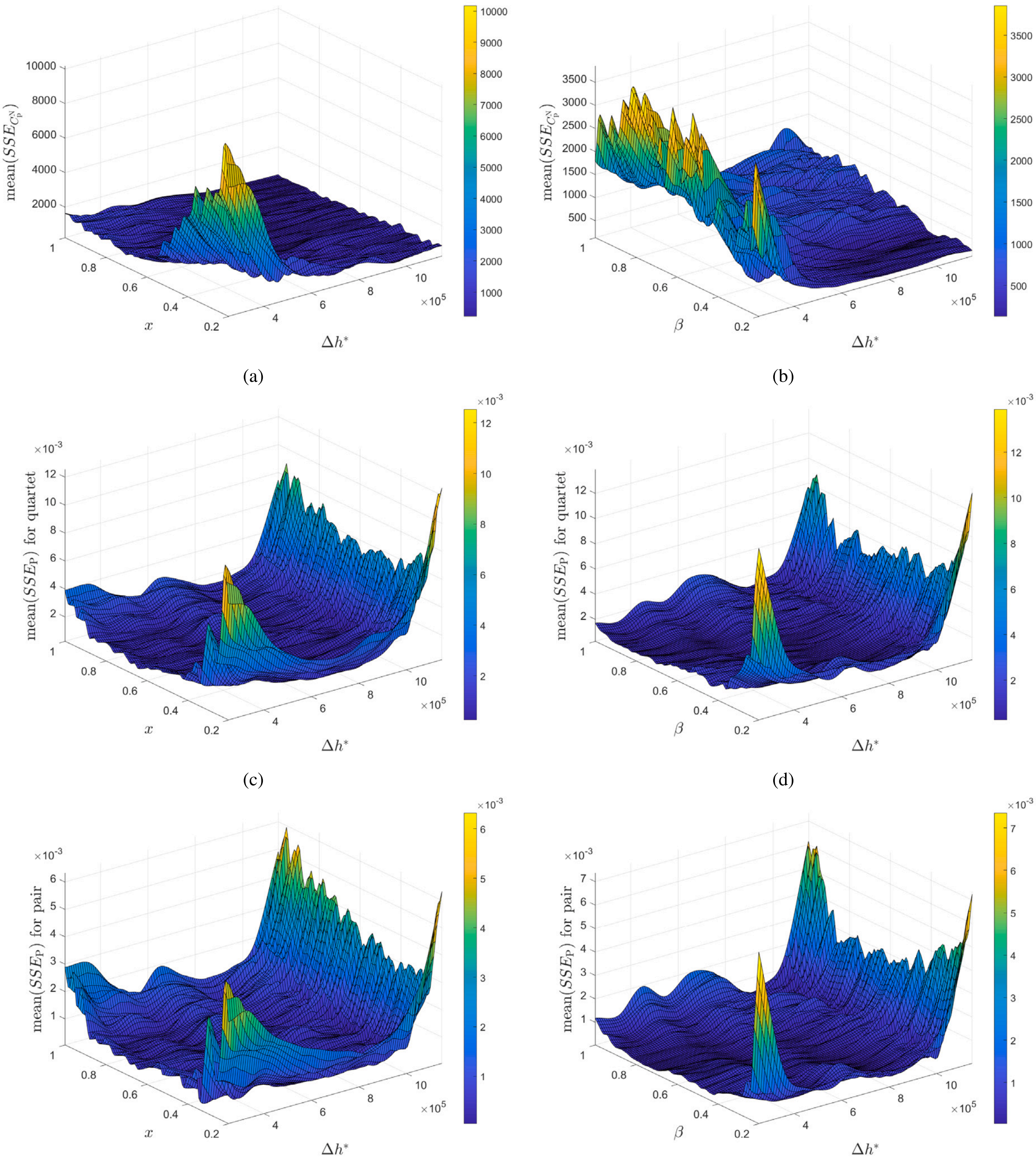

(a) (b) (c) (d) (e) (f)

Fig. 11. G model dependencies on SSE metrics (Eqs. (14) & (15)): $(\Delta h^*, x, SSE)$ (ace); $(\Delta h^*, \beta, SSE)$ (bdf).

x or β lead to a reduction in the recognition ability of the MCNN. This specific region can be described as a region of x-β insensitivity, and as a result, it will generally act as an obstacle to the training process.

The SSE hyperspaces combining Δh^* with either x or β (see Fig. 11ace and Fig. 11bdf, respectively) look rather similar, confirming the dominant influence of Δh^* over both, SSE of the signals and SSE of the parameters. Generally, the relaxation signals are broader at low Δh^*, where the SSE of the signals is highest. The MCNN estimates of the TNM parameters – or more specifically of Δh^* – are the least accurate in the hyperspace corners and on the high-Δh^* hyperspace edge. Corner-wise innacuracy can be explained by a limited ability of MCNN to interpolate from the non-existent neighboring training samples. Innacuracy at the hyperspace edge, on the other hand, can be exaplained by narrow relaxation peaks of the signals, effectively resulting in low X-axis resolution (as discussed in Section 3.2).

3.4. MCNN accuracy vs. real-life applications

To assess the accuracy of the current MCNN estimates in comparison to the demands of real-life scenarios, the outcomes presented in sections such as Absolute Errors and 3D-plotted SSE Metrics will be juxtaposed with findings from recent studies on structural relaxation behavior. These studies provide interpretations of trends in TNM parameters for actual materials. Note that all experimental data and results presented in this section were acquired using either curve-fitting or non-fitting methods, without the utilization of artificial intelligence.

Starting with the polymeric materials, the structural relaxation behavior of poly(p-dioxanone), a semi-crystalline polymer used for the production of biodegradable medical sutures and stents, was studied [62] with dependence on the degree of crystalline content. The apparent activation energy Δh^* was determined with ± 12 kJ mol^{-1} evaluation errors; the parameters x and β were both determined with 0.05 resolution, with the absolute values changing between 0.45–0.80 for x, and between 0.15–0.50 for β. Relaxation behavior of poly(p-dioxanone) was also studied with dependence on the content of the plasticizing monomer [63]. Here, the errors for Δh^* varied in approx. ±5–25 kJ mol^{-1} range; $\log(A/s)$ varied from −104 to −196 in absolute values; determination of x and β with the 0.05 resolution was well sufficient for identification of clear plasticization-induced trends. Comparable accuracy/precision of the TNM parameter determination can be obtained also for the organic low-molecular glasses. Structural relaxation of amorphous indomethacin (anti-inflammatory drug) was studied in dependence on the degree of introduced crystallinity [64,65]. Whereas the individual Δh^* values were determined with the errors in the range of ±5–20 kJ mol^{-1}, a change of $\Delta h^* > 40$ kJ mol^{-1} was identified as the first recognizable deviation from otherwise more-or-less constant Δh^* value as the crystallinity of the indomethacin increased. The x and β parameters were determined in these studies with the 0.01 accuracy, however, only their changes with magnitude > 0.03 were recognized as significantly deviating from the equilibrium scatter. In another study [66] focused on the structural relaxation in the amorphous nimesulide (also a non-steroidal anti-inflammatory drug), the Δh^* values were determined with ±8–12 kJ mol^{-1} errors; the x and β parameters were determined with 0.01 precision.

Slightly worse accuracy of the TNM parameter determination was observed in case of chalcogenide glasses. For example, in the case of the low-T Ge-, As- and Te-doped selenium glasses [67], the activation energy Δh^* was determined with approx. ±10–20 kJ mol^{-1} errors, and the corresponding compositional trends were identified for the changes of $\Delta h^* > 25$ kJ mol^{-1}. The errors of the x and β determination ranged between ±0.02–0.06, with recognizable compositional trends for the 0.05 differences in both x and β; the $\log(A/s)$ errors ranged between ±0.5–4. In case of the GeS_2-Sb_2S_3 and $GeSe_2$-Sb_2Se_3 glasses [68,69], the Δh^* was determined with errors of approx. ±5–20 kJ mol^{-1}, and with identifiable trends for the Δh^* changes above 30 kJ mol^{-1}. The errors of the x and β determination were between ±0.02–0.07 (no significant trends in the evolution of these parameters was observed; the compositional scatter was approx. ±0.05).

The largest errors in the determination of the TNM parameters are usually obtained for the oxide glasses, which exhibit the glass transition at temperatures > 500 °C. The structural relaxation of the Bioglass 45S5 doped with different amounts of CeO_2 was described with Δh^* values having the errors in the ±25–63 kJ mol^{-1} range; the corresponding x and β parameters were estimated with ±0.1 precision. In an akin study for the Li-doped bioglasses, the compositional trends showed scatter within the ±100 kJ mol^{-1} margins for Δh^*, and within the ±0.1 units for x and β. Similar level of (in)accuracy was obtained also for the $MgO-Al_2O_3-P_2O_5$ and $BaO-Al_2O_3-P_2O_5$ glasses [70–72].

Considering the above-listed examples of the TNM parameter determination accuracy for real glassy materials, it is evident that both the corresponding measurement-based as well as evaluation-based errors significantly increase with the materials' T_g. While the accuracy of the present MCNN estimates of x and β is acceptable – being either better or comparable to the errors of real-life measurements and evaluations – across the entire spectrum of relevant non-crystalline materials, it was stated in Section 3.2 that the present MCNN estimates of Δh^* are generally not suitable. However, in light of the information given in the present section, the MCNN models should provide sufficient (comparable with other methodologies) accuracy for the determination of Δh^* in the case of high-T materials.

Despite the promising initial results demonstrated in this study, there are several potential shortcomings that must be acknowledged. One key limitation is that the model was trained and validated exclusively on theoretically simulated data, which inherently lacks the noise and imperfections typically present in experimental datasets. As such, the model's susceptibility to real data was not rigorously tested. Moreover, the MCNN architecture presented here represents a single configuration with a fixed set of hyperparameters, based on preliminary experimentation. While this configuration has proven effective in extracting TNM parameters from datasets introduced in Section 2.1, more systematic approaches to the selection of hyperparameters, such as number of layers, activation function types, learning rate, kernel sizes, and dropout rate, could lead to further improvements in model accuracy and robustness.

4. Conclusions

In this study, the applicability of machine learning for the description and modeling of glass transition kinetics was investigated. Specifically, a multi-scale convolutional neural network was employed for the first time (to the best of authors' knowledge) to estimate the parameters of the Tool-Narayanaswamy-Moynihan model, A, Δh^*, x, and β, using six simulated heating scans derived from a cyclic heat release structural relaxation temperature program. These heating scans, represented as normalized derivative data, correspond to standard outputs obtained through methods such as differential scanning calorimetry.

To facilitate this analysis, a comprehensive state-space of theoretically simulated data was generated, comprising approximately 13.7 million samples and encompassing all practically relevant types of structural relaxation behavior. Subsequently, a set of MCNN models was trained for selected critical regions within the Δh^*-$\log(A)$ state space. This included one model that mapped the entire matrix of Δh^*-$\log(A)$ combinations, although at lower resolution. The results demonstrate that the proposed neural network model effectively extracts the desired values from the input data with high accuracy. Specifically, highly accurate estimates were achieved for the TNM parameters x and β, with accuracies of 90% and 97%, respectively; absolute errors for these estimates were consistently below 0.02. Absolute errors exceeding ±0.05 were observed only in approximately 2% of the β estimates. This level of accuracy is comparable to the standard curve-fitting approach based on non-linear optimization and substantially surpasses the accuracy of all relevant non-fitting methodologies used for determining the TNM parameters x and β.

Conversely, the MCNN estimates for Δh^* and $\log(A)$ were found to be less accurate, with absolute errors approximately in the order of magnitude larger than those achieved by alternative fitting or non-fitting methods. Further analysis of the mutual correlations between TNM parameters and their errors revealed that the most significant errors in Δh^* determination occurred in cases of either high Δh^* combined with low temperature or low Δh^* combined with high temperature – both scenarios being relatively rare in practical materials. Moreover, the generally high magnitude of Δh^* errors becomes less critical for materials with glass transitions at high temperatures, which typically exhibit high Δh^* values, resulting in a proportionally smaller error percentage.

As such, the present research can be considered a pilot study, demonstrating the high potential of the neural networks in the field of the exact modeling of the derivative structural relaxation data. Owing to the remarkable pattern-recognition abilities of neural networks, the present findings represent a very promising basis for the future development of next-gen architectures trained on the real-life-like data (artificially scattered, skewed and noised). Models trained in such manner allow attainment of an objective, accurate and reliable evaluation of the structural relaxation behavior which can be used for practically all types of materials. Such accomplishment would enable a potentially rapid progress in both the structural interpretation of the relaxation parameters and the associated possibilities of chemical fine-tuning of numerous physical properties of glassy materials. This would be an invaluable achievement in the field of materials science.

Based on the present findings, we propose the following steps for the consequent future research:

1. Further optimization of the proposed neural model architecture and base weights of the individual TNM parameters, taking into account current performance and issues.
2. Employment of significantly larger datasets to increase the accuracy of the obtained estimates.
3. Development of a new neural model specialized for the determination of the Δh^* and $\log(A)$ parameters from the different, more suitable types of structural relaxation cyclic experiments.
4. Testing the developed MCNN models on the data with different levels of random scatter added to the base theoretically simulated signal.
5. Testing the developed MCNN models on the data with arbitrarily skewed asymmetry of the relaxation peaks (simulating the thermal inertia effect in thermo-analytical instruments).
6. Comparing the MCNN estimates of TNM parameters obtained for real-life experimental data with the outputs provided for the same data by means of the nowadays most frequently used fitting approaches (e.g., non-linear optimization based on the Levenberg–Marquardt algorithm) and non-fitting methodologies. Considering the results introduced in the present study, a MCNN model fully trained on the theoretical data (as described in the previous five points) should be able to provide similarly good (or even better - in the case of the systemic data-distortions corrupting the curve-fitting procedure) estimates of the TNM parameters as the nowadays standard methods. The ground-truth benchmark methodology used in the case of real-life experimental data should involve the extremely robust simulation-comparative method. Successful verification of the MCNN performance on the real-life experimental data would then ensure a massively more simple, quick, accessible, robust, and unambiguous way of describing the structural relaxation behavior of amorphous materials.

CRediT authorship contribution statement

Marek Pakosta: Writing – review & editing, Writing – original draft, Visualization, Validation, Software, Methodology, Investigation, Funding acquisition, Formal analysis, Data curation, Conceptualization. **Petr Dolezel:** Writing – review & editing, Writing – original draft, Validation, Supervision, Project administration, Methodology, Investigation, Funding acquisition, Formal analysis, Conceptualization. **Roman Svoboda:** Writing – review & editing, Writing – original draft, Validation, Supervision, Methodology, Investigation, Formal analysis, Data curation, Conceptualization.

Declaration of Generative AI and AI-assisted technologies in the writing process

During the preparation of this work the authors used Microsoft Copilot in order to improve language and readability. After using this service, the authors reviewed and edited the content as needed and take full responsibility for the content of the publication.

Declaration of competing interest

The authors declare that they have no known competing financial interests or personal relationships that could have appeared to influence the work reported in this paper.

Acknowledgments

The work was supported from ERDF “Multi-sector and Interdisciplinary Cooperation in Research and Development of Communication, Information and Detection Technologies for Control and Signalling Systems (CIDET)” (No. CZ.02.01.01/00/23_021/0008402).

The work has also been supported by the SGS grant at the Faculty of Electrical Engineering and Informatics, University of Pardubice, Czech Republic.

Appendix A. Supplementary data

Supplementary material related to this article can be found online at https://doi.org/10.1016/j.matchemphys.2024.130107.

Data and software availability

The dataset presented here is a product of highly optimized simulation SW, that is a part of the overall glass transition software suite. This simulation SW that harnesses parallelization and offers a versatile range of settings approximately 30 program options for simulations alone allowing customization to diverse simulation requirements. For more details about the software suite and how to use it, as well as the dataset availability, refer to https://numcraft.eu.

References

[1] L. Berthier, G. Biroli, Theoretical perspective on the glass transition and amorphous materials, Rev. Modern Phys. 83 (2) (2011) 587–645.

[2] C. Rodríguez-Tinoco, M. Gonzalez-Silveira, M. Ramos, J. Rodríguez-Viejo, Ultrastable glasses: new perspectives for an old problem, La Rivista Del Nuovo Cimento 45 (5) (2022) 325–406.

[3] M. Micoulaut, Relaxation and physical aging in network glasses: a review, Rep. Progr. Phys. 79 (6) (2016) 066504.

[4] G. McKenna, S. Simon, 50Th anniversary perspective: challenges in the dynamics and kinetics of glass-forming polymers, Macromolecules 50 (17) (2017) 6333–6361.

[5] V. Novikov, A. Sokolov, Temperature dependence of structural relaxation in glass-forming liquids and polymers, Entropy 24 (8) (2022) 1101.

[6] D. Sidebottom, Coarse-grained model of the glass transition in network-forming oxides, J. Am. Ceram. Soc. 104 (5) (2021) 2007–2016.

[7] Y. Zhang, Crystal-liquid-glass transition and near-unity photoluminescence quantum yield in low melting point hybrid metal halides, J. Am. Chem. Soc. 145 (22) (2023) 12360–12369.

[8] M.E. Pereira, J. Deuermeier, R. Martins, P. Barquinha, A. Kiazadeh, Unlocking neuromorphic vision: Advancements in IGZO-based optoelectronic memristors with visible range sensitivity, ACS Appl. Electron. Mater. 6 (7) (2024) 5230–5243.

[9] S. Yin, B. Zhao, J. Wan, S. Wang, J. Yang, X. Wang, L. Li, Mxene-contact enhanced broadband photodetection in centimeter level ges films, J. Phys. D: Appl. Phys. 55 (26) (2022) 265105.

[10] X. Wang, Z. Li, B. Jin, W. Lu, M. Feng, B. Dong, Q. Liu, H.-J. Yan, S.-M. Wang, D.-J. Xue, Sustainable recycling of selenium-based optoelectronic devices, Adv. Sci. 11 (22) (2024) 2400615.

[11] N. Ma, S. Horike, Metal–organic network-forming glasses, Chem. Rev. 122 (3) (2022) 4163–4203.

[12] R. Henry, In-situ ellipsometry for the determination of thermal transitions and relaxations in organic photovoltaic materials, Chem. Mater. (2023).

[13] T. Ferron, M. Fiori, M. Ediger, D. DeLongchamp, D. Sunday, Composition dictates molecular orientation at the heterointerfaces of vapor-deposited glasses, Jacs Au 3 (7) (2023) 1931–1938.

[14] M. Lee, M. Kim, U. Mangal, J. Seo, J. Kwon, S. Choi, Zinc-modified phosphate-based glass micro-filler improves candida albicans resistance of auto-polymerized acrylic resin without altering mechanical performance, Sci. Rep. 12 (1) (2022).

[15] C. Brütting, J. Dreier, C. Bonten, V. Altstädt, H. Ruckdäschel, Glass transition of PLA-CO2 mixtures after solid-state saturation, J. Cellular Plastics 58 (6) (2022) 917–931.

[16] Y. Zhan, F. Hou, S. Feng, X. Wang, J. Ye, Y. Zhang, The distribution and evolution of refractive index in a polystyrene whispering gallery microcavity during glass transition, Adv. Opt. Mater. 10 (17) (2022) 2102548.

[17] T.L. Nguyen, F. Bédoui, P.-E. Mazeran, M. Guigon, Mechanical investigation of confined amorphous phase in semicrystalline polymers: Case of PET and PLA, Polym. Eng. Sci. 55 (2) (2015) 397–405.

[18] M. Vallet-Regí, A. Salinas, Mesoporous bioactive glasses for regenerative medicine, Mater. Today Bio 11 (2021) 100121.

[19] P. Liu, R. Youngman, L. Jensen, M. Smedskjær, Correlating structure with mechanical properties in lithium borophosphate glasses, Int. J. Appl. Glass Sci. 14 (1) (2022) 38–51.

[20] V. Lubchenko, P. Wolynes, Theory of structural glasses and supercooled liquids, Annu. Rev. Phys. Chem. 58 (1) (2007) 235–266.

[21] Q. Zheng, Y. Zhang, M. Montazerian, O. Gulbiten, J. Mauro, E. Zanotto, Understanding glass through differential scanning calorimetry, Chem. Rev. 119 (13) (2019) 7848–7939.

[22] R. Casalini, C. Roland, Pressure densification of a simple liquid, J. Non-Cryst. Solids 475 (2017) 25–27.

[23] A. Tool, Relation between inelastic deformability and thermal expansion of glass in its annealing range, J. Am. Ceram. Soc. 29 (1946) 240–253.

[24] O. Narayanaswamy, A model of structural relaxation in glass, J. Am. Ceram. Soc. 54 (1971) 491–497.

[25] C. Moynihan, A. Easteal, M. DeBolt, J. Tucker, Dependence of the fictive temperature of glass on cooling rate, J. Am. Ceram. Soc. 59 (1976) 12–16.

[26] G.W.H. Höhne, W.F. Hemminger, H.-J. Flammersheim, Differential Scanning Calorimetry, Springer-Verlag Berlin Heidelberg, 2003.

[27] A.J. Kovacs, Transition vitreuse dans les polymères amorphes. Etude phénoménologique, in: Fortschritte Der Hochpolymeren-Forschung, Springer Berlin Heidelberg, Berlin, Heidelberg, 1964, pp. 394–507.

[28] R. Svoboda, J. Málek, Description of macroscopic relaxation dynamics in glasses, J. Non-Cryst. Solids 378 (2013) 186–195.

[29] P. Honcová, P. Košťál, M. Včeláková, R. Svoboda, G. Sadovská, J. Barták, J. Málek, Structural interpretation of the viscous flow and relaxation kinetics in the as-se and ge-se chalcogenide systems, J. Non-Cryst. Solids 643 (2024).

[30] R. Kaur, S. Singh, A comprehensive review of object detection with deep learning, Digital Signal Process. Rev. J. 132 (2022).

[31] P. Payal, M.M. Goyani, A comprehensive study on face recognition: methods and challenges, Imaging Sci. J. 68 (2) (2020) 114–127.

[32] X. Chen, X. Wang, K. Zhang, K.-M. Fung, T.C. Thai, K. Moore, R.S. Mannel, H. Liu, B. Zheng, Y. Qiu, Recent advances and clinical applications of deep learning in medical image analysis, Med. Image Anal. 79 (2022).

[33] S. Fu, L. Wang, S. Moon, N. Zong, H. He, V. Pejaver, R. Relevo, A. Walden, M. Haendel, C.G. Chute, H. Liu, Recommended practices and ethical considerations for natural language processing-assisted observational research: A scoping review, Clinical Translat. Sci. 16 (3) (2023) 398–411.

[34] S. Mozaffari, O.Y. Al-Jarrah, M. Dianati, P. Jennings, A. Mouzakitis, Deep learning-based vehicle behavior prediction for autonomous driving applications: A review, IEEE Trans. Intell. Transp. Syst. 23 (1) (2022) 33–47.

[35] D. Mohanty, A.K. Parida, S.S. Khuntia, Financial market prediction under deep learning framework using auto encoder and kernel extreme learning machine, Appl. Soft Comput. 99 (2021).

[36] K. Ng, Y. Huang, C. Koo, K. Chong, A. El-Shafie, A. Najah Ahmed, A review of hybrid deep learning applications for streamflow forecasting, J. Hydrol. 625 (2023).

[37] M. Soori, B. Arezoo, R. Dastres, Artificial intelligence, machine learning and deep learning in advanced robotics, a review, Cognit. Robotics 3 (2023) 54–70.

[38] S. Shahriar, GAN computers generate arts? A survey on visual arts, music, and literary text generation using generative adversarial network, Displays 73 (2022).

[39] S.W. Chen, S.L. Wang, X.Z. Qi, S.M. Samuri, C. Yang, Review of ECG detection and classification based on deep learning: Coherent taxonomy, motivation, open challenges and recommendations, Biomed. Signal Process. Control 74 (2022).

[40] Q. Zhang, D. Zhou, X. Zeng, HeartID: A multiresolution convolutional neural network for ECG-based biometric human identification in smart health applications, IEEE Access 5 (2017) 11805–11816.

[41] N. Liu, Y. Long, C. Zou, Q. Niu, L. Pan, H. Wu, Adcrowdnet: An attention-injective deformable convolutional network for crowd understanding, Proc. IEEE Comput. Soc. Conf. Comput. Vis. Pattern Recogn. 2019-June (2019) 3220–3229.

[42] N.V. Muravyev, G. Luciano, H.L. Ornaghi, R. Svoboda, S. Vyazovkin, Artificial neural networks for pyrolysis, thermal analysis, and thermokinetic studies: The status quo, Molecules 26 (2021) 3727.

[43] N. Bhuyan, R. Narzari, S.M.B. Baruah, R. Kataki, Comparative assessment of artificial neural network and response surface methodology for evaluation of the predictive capability on bio-oil yield of tithonia diversifolia pyrolysis, Biomass Conv. Bioref. (2020).

[44] M. Al-Yaari, I. Dubdub, Application of artificial neural networks to predict the catalytic pyrolysis of HDPE using non-isothermal TGA data, Polymers 12 (2020) 1813.

[45] J. Farah, R. Cavalcanti, J. Guimarães, C. Balthazar, P. Coimbra, T. Pimentel, E. Esmerino, M. Duarte, M. Freitas, D. Granato, et al., Differential scanning calorimetry coupled with machine learning technique: An effective approach to determine the milk authenticity, Food Control 121 (2021) 107585.

[46] B. Rojek, B. Suchacz, M. Wesolowski, Artificial neural networks as a supporting tool for compatibility study based on thermogravimetric data, Thermochim. Acta 659 (2018) 222–231.

[47] E. Epure, S. Oniciuc, N. Hurduc, E.D. agoi, Artificial neural network modeling of glass transition temperatures for some homopolymers with saturated carbon chain backbone, Polymers (Basel) 13 (2021) 4151.

[48] D. Viatkin, M. Zakharov, D. Zhuro, Prediction of reduced glass transition temperature of metallic alloys based on a neural network, J. Phys. Conf. Series 2373 (2022) 082016.

[49] A. Alesadi, Z. Cao, Z. Li, S. Zhang, H. Zhao, X. Gu, W. Xia, Machine learning prediction of glass transition temperature of conjugated polymers from chemical structure, Cell Rep. Phys. Sci. 3 (2022) 100911.

[50] T. Nguyen, M. Bavarian, A machine learning framework for predicting the glass transition temperature of homopolymers, Ind. Eng. Chem. Res. 61 (2022) 12690–12698.

[51] A. Banerjee, A. Iscen, K. Kremer, O. Kukharenko, Determining glass transition in all-atom acrylic polymeric melt simulations using machine learning, J. Chem. Phys. 159 (2023) 074108.

[52] S. Nolan, A. Smerzi, L. Pezzè, A machine learning approach to Bayesian parameter estimation, npj Quantum Inf. 7 (1) (2021).

[53] I.M. Hodge, A.R. Berens, Effects of annealing and prior history on enthalpy relaxation in glassy polymers. 2. Mathematical modeling, Macromolecules 15 (3) (1982) 762–770.

[54] X. Shao, C.S. Kim, D.G. Kim, Accurate multi-scale feature fusion CNN for time series classification in smart factory, CMC-Comput. Mater. Contin. 65 (1) (2020) 543–561.

[55] W. Chen, K. Shi, Multi-scale attention convolutional neural network for time series classification, Neural Netw. 136 (2021) 126–140.

[56] L. Wu, N. Sang, J. Yang, L. Jing, C. Gao, L. Li, Densenet-based multi-scale recurrent network for video restoration with Gaussian blur, in: Y. Zhao, N. Barnes, B. Chen, R. Westermann, X. Kong, C. Lin (Eds.), IMAGE and GRAPHICS, ICIG 2019, PT I, in: Lecture Notes in Computer Science, vol. 11901, Tsinghua Univ; Peking Univ; CAS, Inst Automat, 2019, pp. 582–594, 10th International Conference on Image and Graphics (ICIG), China Soc Image & Graph, Beijing, PEOPLES R CHINA, AUG 23-25, 2019.

[57] N. Taghinezhad, M. Yazdi, A new unsupervised video anomaly detection using multi-scale feature memorization and multipath temporal information prediction, IEEE Access 11 (2023) 9295–9310.

[58] G. Habib, S. Qureshi, Optimization and acceleration of convolutional neural networks: A survey, J. King Saud Univ. Comput. Inf. Sci. 34 (7) (2022) 4244–4268.

[59] R. Svoboda, J. Málek, Enthalpy relaxation in ge-se glassy system, J. Therm. Anal. Cal. 113 (2013) 831–842.

[60] J.M. Hutchinson, A.J. Kovacs, Effects of thermal history on structural recovery of glasses during isobaric heating, Polym. Eng. Sci. 24 (1984) 1087–1093.

[61] R. Svoboda, Novel equation to determine activation energy of enthalpy relaxation, J. Therm. Anal. Calorim. 121 (2015) 895–899.

[62] R. Svoboda, J. Machotová, M. Krbal, D. Jezbera, M. Nalezinková, J. Loskot, A. Bezrouk, Complex thermokinetic characterization of polydioxanone for medical applications: Conditions for material processing, Polymer 277 (2023) 125978.

[63] R. Svoboda, J. Machotova, S. Podzimek, P. Honcova, M. Chromcikova, M. Nalezinkova, J. Loskot, A. Bezrouk, D. Jezbera, How temperature-induced depolymerization and plasticization affect the process of structural relaxation, Polymer 290 (2023) 126549.

[64] R. Svoboda, D. Košťálová, M. Krbal, A. Komersová, Indomethacin: The interplay between structural relaxation, viscous flow and crystal growth, Molecules 27 (2022) 5668.

[65] R. Svoboda, M. Pakosta, P. Doležel, How the presence of crystalline phase affects structural relaxation in molecular liquids: The case of amorphous indomethacin, Int. J. Mol. Sci. 24 (2023) 16275.

[66] R. Svoboda, J. Macháčková, M. Nevyhoštěná, A. Komersová, Thermal stability of amorphous nimesulide: From glass formation to crystal growth and thermal degradation, Phys. Chem. Chem. Phys. (2023).

[67] R. Svoboda, Relaxation processes in se-rich chalcogenide glasses: Effect of characteristic structural entities, Acta Mater. 61 (2013) 4534–4541.

[68] R. Svoboda, J. Málek, M. Liška, Correlation between the structure and relaxation dynamics of (GeS2)y(sb2s3)1-y glassy matrices, J. Non-Cryst. Solids 479 (2018) 113–119.

[69] R. Svoboda, J. Málek, M. Liška, Correlation between the structure and structural relaxation data for (GeSe2)y(Sb2Se3)1-y glasses, J. Non-Cryst. Solids 505 (2019) 162–169.

[70] R. Svoboda, M. Chromčíková, B. Hruška, M. Liska, Correlation between the activation energies of structural relaxation and viscous flow for BaO–P2O5–Al2O3 glasses, J. Non-Cryst. Solids 536 (2020) 119998.

[71] M. Chromčíková, B. Hruška, A. Nowicka, R. Svoboda, M. Liška, Role of modifiers in the structural interpretation of the glass transition behavior in MgO/BaO-Al2O3-P2O5 glasses, J. Non-Cryst. Solids 573 (2021) 121114.

[72] M. Chromčíková, B. Hruška, A. Nowicka, R. Svoboda, M. Liska, Structural relaxation and viscosity of al2o3 doped magnesium phosphate glasses, J. Non-Cryst. Solids 550 (2020) 120323.

Marek Pakosta earned his B.S. degree in Process Control in 2019 and his M.S. degree in Automatic Control from the University of Pardubice, Czech Republic, in 2021. He is currently pursuing a Ph.D., focusing on modeling the structural relaxation behavior of amorphous materials through the application of deep learning.

He has authored two papers and co-authored one. His research interests encompass computer science, artificial intelligence, and structural relaxation. Specializing as a C++ software developer, he has contributed to the development of several real-time applications, some of which are utilized by the air navigation services of the Czech Republic, city police, and the public transport company of Pardubice. Presently, he works as an optical software developer in the automotive industry.

Petr Dolezel received his Ph.D. degree from the University of Pardubice, Czech Republic, in 2009. Then, in 2024, he defended his full professorship at Tomas Bata University and at present, he works as a professor and the dean at the Faculty of Electrical Engineering and Informatics, University of Pardubice. His research interests include neural and evolutionary computation in process control, and signal and image processing. He is the author of more than 100 scientific contributions, including 20 journal papers and lectures at CORE-ranked conferences. In addition, he has been a leader or member of research teams for a dozen research and development projects. As an academician, he led 5 Ph.D. students to a successful defense of their dissertations. He is a member of the Technical Program Committee of several international conferences and is an active reviewer for numerous scientific journals. He intensively cooperates with research teams at the University of Burgos, Spain, and at the Slovak University of Technology, Slovakia.

Roman Svoboda received M.Sc. in inorganic technology from the University of Pardubice in 2004. He completed his PhD in physical chemistry in 2008, and in 2020 he was appointed the independent researcher in physical chemistry (a scientific version of Assoc. Prof. – degree specific for the University of Pardubice). He has co-authored more than 150 papers in impacted journals, with over 1100 citation and h-index of 17 (self-citations excluded) and is included between the “World’s top 2 % most cited scientists” (Stanford Univ. & Elsevier). Roman Svoboda specializes in thermoanalytical, spectroscopic and microscopic techniques. He is focused on advanced solid-state kinetics, theory of amorphous materials, structural relaxation kinetics in the glass transition region, crystal growth in thin amorphous films, and dissolution of amorphous drugs.